HHS Public Access

Author manuscript

Cell Metab. Author manuscript; available in PMC 2024 October 03.

Published in final edited form as:

Cell Metab. 2023 October 03; 35(10): 1782–1798.e8. doi:10.1016/j.cmet.2023.07.009.

NSUN2 Is a Glucose Sensor Suppressing cGAS/STING to Maintain Tumorigenesis and Immunotherapy Resistance

Tingjin Chen[1,5], **Zhi-Gang Xu**[3], **Jie Luo**[1], **Rajesh Kumar Manne**[1,5], **Zhengyu Wang**[2], **Che-Chia Hsu**[1,5], **Bo-Syong Pan**[1,5], **Zhen Cai**[1], **Pei-Jane Tsai**[1], **Yau-Sheng Tsai**[1], **Zhong-Zhu Chen**[3], **Hongyu Li**[2], **Hui-Kuan Lin**[1,4,5,*]

[1]Department of Cancer Biology, Wake Forest Baptist Medical Center, Wake Forest University, Winston-Salem, NC 27101, USA

[2]University of Arkansas for Medical Sciences, College of Pharmacy, Division of Pharmaceutical Science, 200 South Cedar, Little Rock, AR 72202, USA.

[3]Chongqing Engineering Laboratory of Targeted and Innovative Therapeutics, Chongqing Key Laboratory of Kinase Modulators as Innovative Medicine, IATTI, Chongqing University of Arts and Sciences, Yongchuan, Chongqing 402160, China

[4]LEAD CONTACT

SUMMARY

Glucose metabolism is known to orchestrate oncogenesis. Whether glucose serves as a signaling molecule directly regulating oncoprotein activity for tumorigenesis remains elusive. Here, we report that glucose is a cofactor binding to methyltransferase NSUN2 at amino acid 1–28 to promote NSUN2 oligomerization and activation. NSUN2 activation maintains global m^5C RNA methylation including *TREX2* and stabilizes *TREX2* to restrict cytosolic dsDNA accumulation and cGAS/STING activation for promoting tumorigenesis and anti-PD-L1 immunotherapy resistance. A NSUN2 mutant defective in glucose binding or disrupting glucose/NSUN2 interaction abolishes NSUN2 activity and TREX2 induction leading to cGAS/STING activation for oncogenic suppression. Strikingly, genetic deletion of the glucose/NSUN2/TREX2 axis suppresses tumorigenesis and overcomes anti-PD-L1 immunotherapy resistance in those cold tumors through cGAS/STING activation to facilitate apoptosis and $CD8^+$ T cell infiltration. Our study identifies NSUN2 as a direct glucose sensor whose activation by glucose drives tumorigenesis and immunotherapy resistance by maintaining TREX2 expression for cGAS/STING inactivation.

[*]Correspondence: hui-kuan.lin@duke.edu.

[5]Present address: Department of Pathology, Duke University School of Medicine, Durham, NC 27710, USA

AUTHOR CONTRIBUTIONS

T.C. and H.K.L. designed experiments and wrote the manuscript. T.C. performed experiments and analyzed the data. Z.-G.X, Z.W., and Z.-Z.C help synthesize biotin-glucose and biotin-2DG. J.L., R.K.M., C.C.H., B.S.P., Z.C., P.J.T., Y.S.T., and H.Y.L provided technical support, comments, and suggestions.

DECLARATION OF INTERESTS

H.K.L. is a consultant for Stablix, Inc. All other authors have declared that no competing interests exist.

eTOC blurb

Whether glucose is a signaling molecule directly regulating oncoproteins for tumorigenesis remains elusive. Chen et al. identify NSUN2 as a direct glucose sensor driving tumorigenesis and immunotherapy resistance by maintaining TREX2 expression for cGAS/STING inactivation, thus opening a new avenue for studying novel glucose's actions in regulating diverse biological processes.

Graphical Abstract

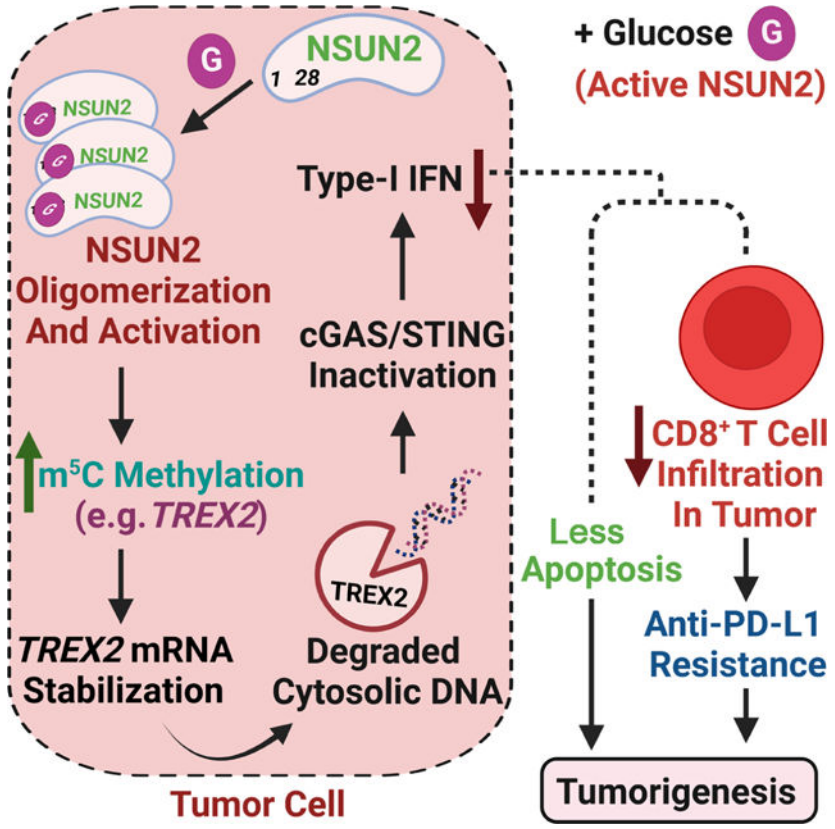

INTRODUCTION

Cancers display highly distinct metabolic states compared with normal cells. Enhanced aerobic glycolysis known as Warburg effect is observed in most cancer types and is associated with cancer stem cell maintenance, cancer progression and metastasis, and drug resistance [1–4]. Glucose is a key nutrient for glycolysis, whose uptake to cancer cells is elevated compared to normal cells partly through increased expression of glucose transporters in cancer cells [5]. Hexokinase (HK) is a rate limiting enzyme mediating the first step of glycolysis for tumorigenesis [6]. Glycolysis not only provides key energy sources but also building blocks and redox homeostasis for cancer cell proliferation and survival leading to cancer progression [6,7].

In addition to fueling cancer growth and survival through glycolysis and TCA cycle [8], glucose also drives global histone H3 acetylation for its oncogenic activity through acetyl-CoA production [9–12] and histone H3 ubiquitination [13]. These studies establish the well-recognized dogma that glucose maintains its oncogenic activity primarily through glucose metabolism. However, it remains unclear whether glucose can act as a signaling molecule directly binding to its protein targets for maintaining oncogenic processes independently of glucose metabolism. Notably, an earlier study revealed that glucose could trigger mitogen-activated protein kinase activation in adipocytes likely independent of glucose metabolism [14], raising the possibility that glucose may act through its direct sensor to orchestrate its oncogenic processes. In this study, we aimed to identify a direct target of glucose that mediates its oncogenic activity for tumorigenesis and immunotherapy resistance.

RESULTS

NSUN2 Is a Novel Interacting Protein of Glucose, and Its N-terminal Region Mediates Glucose Binding

To identify direct glucose sensors, we synthesized biotin-labeled glucose, incubated it with cell lysate from HEK293 cells and pulled down potential glucose interacting proteins with streptavidin beads, followed by systematic mass spectrometry analysis (Figure 1A). Several proteins that potentially interact with biotin-glucose, but not biotin, were identified from mass spectrometry analysis (Table S1). We selected NSUN2 for further characterization and study, as NSUN2, an RNA 5-methylcytosine (m^5C) methyltransferase triggering m^5C RNA methylation including mRNA and tRNA to orchestrate RNA stability, was recently identified as an oncoprotein promoting m^5C RNA methylation of diverse targets such as *HGDF* [15–18] and is overexpressed in numerous human cancers [15]. We verified the interaction of NSUN2 with glucose through biotin and biotin-glucose incubated with cell lysates from diverse cell lines, and such interaction was disrupted by adding unlabeled glucose (Figure 1B and 1C; Figure S1A). As a positive control for our assay, we demonstrated that biotin-glucose could bind to DDX21 [19], and this interaction could be abrogated by unlabeled glucose, indicating that our approach can be used to identify potential glucose binding proteins (Figure S1B and S1C). We then performed an *in vitro* binding assay using recombinant NSUN2 proteins to assess the direct interaction between glucose and NSUN2. Figure 1D and 1E revealed that biotin-glucose directly interacts with NSUN2, which consists of three isoforms including NSUN2-F1 (amino acid (aa) 1–767), NSUN2-F2 (aa 85–120: SHAKEILHCLKNKYFKELEDLEVDGQKVEVPQPLSW → R) and NSUN2-F3 (Δ aa 1–236) (Figure S1D–S1F) [20]. Notably, glucose directly interacts with NSUN2-F1 and NSUN2-F2, but not NSUN2-F3 (Figure 1D and 1E), indicating that NSUN2 aa 1–236, but not aa 85–120 and aa 237–767, is required for glucose binding.

To gain further insight into the detailed region of NSUN2 binding to glucose, we further generated various NSUN2 truncated mutants from the N-terminal region of NSUN2 (aa 1–236) and subjected them to *in vitro* glucose binding assays (Figure S1G). The NSUN2 mutant with aa 1–84 deletion, but not other mutants, failed to interact with glucose, indicating the requirement of aa 1–84 of NSUN2 for glucose binding (Figure 1F and 1G). We further generated three mutants of NSUN2 from aa 1–84 (Figure S1H and S1I) and

found that the NSUN2 mutant with deletion of aa 1–28, but not the other mutants, no longer interacted with glucose (Figure 1H and 1I), suggesting that aa 1–28 of NSUN2 is likely a region for glucose binding. To validate this notion further, we generated a cell-penetrating TAT-N28 peptide and a control TAT peptide by fusing aa 1–28 from NSUN2 or a control peptide randomly swapped from NSUN2 aa 1–28 with a trans-activator of transcription (TAT) tag placed in its N-terminal region (Figure 1J), allowing for the peptide to get into the cells [21,22]. As expected, the TAT-N28 peptide, but not the control TAT peptide, could directly interact with glucose (Figure 1K). Remarkably, the TAT-N28 peptide disrupted *in vitro* glucose/NSUN2 binding in a dose-dependent manner (Figure 1L). Collectively, these data suggest that glucose directly binds to NSUN2 at aa 1–28 and the TAT-N28 peptide could abolish glucose/NSUN2 binding.

Interestingly, by blasting NSUN2 N28 peptide against 40 other potential glucose interacting proteins identified from mass spectrometry analysis (Table S1), we found that the motif (RRSR) observed in the NSUN2 N28 peptide also appears in some of these proteins including SRSF8, U2AF2, SRSF10, and LUC7L (Table S2). It will be interesting to know whether glucose can also bind to these proteins via the motif (RRSR) in a future follow-up study.

Glucose Serves As a Cofactor to Directly Promote Oligomerization and Activation of NSUN2

Global m^5C RNA methylation is mediated by DNA methyltransferase 2 (DNMT2) and NOP2/SUN RNA methyltransferase family members (NSUN) [23–26]. We demonstrated that NSUN2 is a primary enzyme mediating global m^5C RNA methylation in various cancer cell lines, since *NSUN2* knockdown impaired global m^5C RNA methylation in a Dot blot assay (Figure S2A–S2D). Since glucose directly interacts with NSUN2, we assessed whether glucose could impact NSUN2 m^5C RNA methyltransferase activity. Notably, glucose deprivation in these cancer cell lines markedly impaired m^5C RNA methylation levels indicative of defective NSUN2 activity, and adding back glucose at physiological levels (5.5 mM) rescued the defect in m^5C RNA methylation levels (Figure 2A–2C; Figure S2E). Importantly, the restored effect on m^5C RNA methylation levels by glucose depends on the presence of NSUN2 (Fig 2D; Figure S2F and S2G). Surprisingly, adding 2-Deoxy-D-glucose (2DG), a glucose derivative that cannot be metabolized by HK and serves as a HK/glycolysis inhibitor [27], at 5.5 mM also rescued the defect in m^5C RNA methylation levels (Figure 2E; Figure S2H). Similar to biotin-glucose, biotin-2DG could also bind to NSUN2, and such interaction was disrupted by the unlabeled 2DG (Figure 2F–2H). Thus, glucose metabolism is likely dispensable for glucose's effect on regulating NSUN2 activity. In support of this notion, blocking glucose metabolism toward glycolysis by HK2 knockdown, a key isoform of HK frequently overexpressed in cancer cells [6], failed to block glucose's effect of rescuing m^5C RNA methylation levels. We noticed that HK2 loss even enhanced the effect of glucose on rescuing m^5C RNA levels (Figure 2I; Figure S2I–S2K), presumably due to glucose accumulation caused by the failure in glucose metabolism upon HK2 loss. Moreover, NSUN2 overexpression cooperated with glucose to promote m^5C RNA methylation levels (Figure 2J; Figure S2L–S2N). Remarkably, disrupting glucose/NSUN2 binding by the TAT-N28 peptide impaired m^5C RNA methylation levels in

a dose-dependent manner (Figure 1L; Figure 2K; Figure S2O). Collectively, these results suggest that glucose maintains global m^5C RNA methylation and NSUN2 activity *in vivo* through glucose/NSUN2 binding independently of its metabolism.

Importantly, glucose exhibited a dose-dependent effect to directly promote *in vitro* NSUN2 methyltransferase activity in an *in vitro* m^5C RNA methylation assay using recombinant NSUN2 proteins along with glucose (Figure 2L). It is also important to note that glucose at physiological levels enhanced NSUN2 activity more than 3-fold compared to vehicle control (Figure 2L and 2M). Consistently, 2DG also promoted NSUN2 activity *in vitro*, like glucose did (Figure 2M). However, the downstream metabolite products of glucose including glucose-6- phopshate (G6P), fructose 1, 6-biphosphate (FBP), fructose 6-phopshate (F6P), myo-inositol (Ins), and pyruvate (Pyr) [6,28] displayed either no effect or only a modest effect on promoting NSUN2 activity (Figure 2M). Thus, glucose directly promotes NSUN2 methyltransferase activity *in vitro* independently of its metabolism.

We present two lines of evidence to further support the role of glucose/NSUN2 binding in promoting NSUN2 activity *in vitro*. First, glucose failed to enhance the activity of the NSUN2 mutant (Δ aa 1–28), defective in glucose binding, while it promoted the activity of another NSUN2 deletion mutant that could still bind to glucose (Figure 1I; Figure 2N). Second, disrupting glucose/NSUN2 binding by the TAT-N28 peptide impaired the effect of glucose on promoting NSUN2 activity both *in vivo* and *in vitro* (Figure 1L; Figure 2K and 2O; Figure S2O). Collectively, glucose serves as a cofactor that directly binds to NSUN2 at aa 1–28 to promote NSUN2 methyltransferase activity.

Protein dimerization and oligomerization processes have been shown to play a crucial step for activation of diverse enzymes such as HK [29,30] and PKM2 [31,32]. We then determined whether glucose may impact NSUN2 dimerization/oligomerization levels, thus explaining why glucose promotes NSUN2 activity. Notably, NSUN2 oligomerization examined by the native gel approach was markedly enhanced by glucose in a dose-dependent manner using recombinant NSUN2 proteins (Figure 2P and 2Q). It is important to note that we failed to detect the monomer of NSUN2 under this native gel approach, but glucose did not increase total NSUN2 protein levels under the SDS denatured condition, which detects all forms of NSUN2 (Figure 2P). To validate this notion further, we conducted a chemical cross-linking assay and found that glucose induced NSUN2 oligomerization but reduced NSUN2 monomer and dimer in a dose-dependent manner (Figure 2R–2U). Remarkably, glucose failed to promote the oligomerization of the NSUN2 mutant (Δ aa 1–28) (Figure 2V and 2W), correlating with the defect in promoting NSUN2 activity by glucose (Figure 2N). Furthermore, disrupting glucose/NSUN2 binding by the TAT-N28 peptide abrogated glucose-mediated NSUN2 oligomerization (Figure 2X and 2Y), correlating with the impairment of glucose effect on promoting NSUN2 activity (Figure 2K and 2O; Figure S2O). Thus, glucose/NSUN2 binding directly promotes NSUN2 oligomerization and activity.

Glucose/NSUN2 Binding Leading to NSUN2 Activation Maintains Oncogenic Activity of Cancer Cells

Glucose maintains cancer cell proliferation, survival, and cancer stemness critical for cancer development [13]. Consistently, glucose deprivation leading to defective NSUN2 activity impaired cancer stemness of various cancer cells as determined by cancer sphere assay, and adding back glucose rescued this defect (Figure 3A; Figure S3A). To assess whether glucose metabolism is sufficient for mediating the oncogenic processes of glucose, we performed viability and sphere assays in cancer cells under glucose deprivation and added back G6P (by transfection) [33] with or without the non-metabolizable glucose analog, 2DG or 3-O-methyl-D-glucose (3OMG) [19]. Surprisingly, adding back G6P, 2DG or 3OMG alone, is not sufficient for rescuing the defect in cancer sphere and colony formation (Figure 3B and 3C; Figure S3B and S3C). Strikingly, the combination of G6P with either 2DG or 3OMG fully rescued these defects (Figure 3C; Figure S3C). Thus, glucose metabolism is not sufficient for glucose-mediated oncogenic processes, and direct glucose action is necessary for maintaining these biological processes.

Similar to glucose deprivation, NSUN2 knockdown also impaired cancer cell survival, proliferation and cancer stemness, correlating with reduced expression of cancer stem cell factors, OCT4 and SOX2 (Figure 3D–3G; Figure S3D–S3H). Notably, loss of NSUN2 compromised the tumorigenicity of Hep3B and PC3 cells in an *in vivo* xenograft tumorigenesis assay (Figure 3H; Figure S3I), indicating the oncogenic role of NSUN2 in these cancer cell lines.

We then assess whether glucose/NSUN2 binding for NSUN2 activation serves as a key mechanism to maintain oncogenic processes. Remarkably, the TAT-N28 peptide disrupting glucose/NSUN2 binding lead to impaired NSUN2 activity significantly reducing oncogenic properties including cancer cell proliferation, survival and cancer stemness (Figure 3I–3K; Figure S3J–S3L). However, these effects do not appear to result from affecting ATP levels, since the TAT-N28 peptide failed to block glucose-mediated ATP production (Figure S3M). Restoration of NSUN2, but not the NSUN2 mutant (Δ aa 1–28), rescued the defect in these oncogenic properties in NSUN2 knockdown cancer cells, correlating with the expression of OCT4 and SOX2 (Figure 3L–3R; Figure S3N). Furthermore, glucose restoration rescued cancer cell survival upon glucose deprivation, but loss of NSUN2 or impaired glucose/NSUN2 binding abrogated glucose's rescued effect (Figure 3Q). In a xenograft tumorigenesis assay, NSUN2, but not the NSUN2 mutant (Δ aa 1–28), rescued the defect in tumorigenicity upon NSUN2 knockdown (Figure 3R). Collectively, our data suggest that glucose/NSUN2 binding drives NSUN2 activation and critically maintains oncogenic activity of cancer cells.

The Glucose/NSUN2 Axis Maintains TREX2 Expression to Execute Its Oncogenic Activity

NSUN2 methyltransferase triggers m^5C RNA methylation and stability of its RNA targets. In a bladder cancer cell model, NSUN2 triggered m^5C RNA methylation and stability of *HDGF* mRNA, leading to the promotion of bladder cancer development [16]. Therefore, we conducted systematic RNA sequencing (RNA-seq) along with RNA immunoprecipitation (RNA-IP) to dissect the m^5C RNA methylation targets of glucose/NSUN2 responsible for

its oncogenic activity. RNA-seq revealed that 122 genes were induced by glucose in a NSUN2-dependent manner (Figure 4A; Table S3). We confirmed the RNA-seq results for some of these targets, such as *TREX2*, *HNF4A*, *SREBF1*, *HES2*, and *NEUROD2*, by real time qPCR (Figure 4B; Figure S4A). Immunoblotting assays further demonstrated that the protein expression of these targets was induced by the glucose/NSUN2 axis (Figure 4C–4G; Figure S4B–S4J). Glucose induced *TREX2* mRNA expression in control and NSUN2 knockdown cells restored with NSUN2, but not in NSUN2 knockdown cells restored with the NSUN2 mutant (Δ aa 1–28) (Figure 4H). Thus, glucose induces NSUN2 activation to maintain RNA and protein expression of a subset of its targets.

Using RNA-IP to assess m^5C RNA methylation in these affected genes by the glucose/NSUN2 axis, we found that only *TREX2*, but not other targets, consistently underwent m^5C RNA methylation in a manner dependent on both glucose and NSUN2 (Figure 4I; Figure S4K). Glucose induced m^5C RNA levels of *TREX2* in control and NSUN2 knockdown cells restored with NSUN2, but not in NSUN2 knockdown cells restored with the NSUN2 mutant (Δ aa 1–28) (Figure 4I, 4J). Notably, blocking glucose/NSUN2 binding by the TAT-N28 peptide impaired glucose-induced m^5C RNA levels of *TREX2* (Figure 4J). Thus, glucose/NSUN2 binding appears to be critical for inducing m^5C RNA methylation of *TREX2*.

TREX2 exhibits an exonuclease activity that degrades single strand DNA (ssDNA) and double strand DNA (dsDNA) similar to its closely related protein, TREX1 [34,35]. TREX1 is a key repressor for the cGAS/STING pathway involved in cancer and immune regulation [36–39]. We selected the *TREX2* gene among these targets to further characterize its involvement in glucose/NSUN2-mediated oncogenic processes. The mRNA and protein expression of *TREX2* was induced by glucose in various cancer cells in a NSUN2-dependent manner, and NSUN2 overexpression promoted mRNA and protein expression of *TREX2* (Figure 4A–4H; Figure S4E–S4J; Figure S4L). Induction of mRNA and m^5C RNA methylation levels of *TREX2* by glucose strictly depends on NSUN2 and glucose/NSUN2 binding (Figure 4G–4I; Figure S4M–S4P). Notably, restoration of NSUN2, but not of the NSUN2 mutant (Δ aa 1–28), rescued the defect in mRNA and protein expression and m^5C RNA methylation levels of *TREX2* in NSUN2 knockdown cells (Figure 4G–4I). Moreover, disrupting glucose-NSUN2 interaction by the TAT-N28 peptide impaired *TREX2* m^5C RNA methylation and protein induction by glucose (Figure 4J and 4K). In line with the results for m^5C RNA methylation of *TREX2*, both glucose deprivation and NSUN2 loss markedly reduced *TREX2* mRNA stability, but not mRNA stability of *ACTIN* and *NSUN2* (Figure 4L; Figure S5A), which was rescued by glucose or NSUN2 restoration, but not by the NSUN2 mutant (Δ aa 1–28). Conversely, NSUN2 overexpression promoted *TREX2,* but not *ACTIN* and *NSUN2*, mRNA stability (Figure 4M; Figure S5B). RNA-IP assays revealed that the region (aa 85–120) within N-terminal domain (NTD) of NSUN2 is required for NSUN2 binding to *TREX2* mRNA (Figure 4N and 4O; Figure S5C), consistent with the earlier study showing that NSUN2 binds to its target mRNA through its NTD [40]. The glucose/NSUN2 axis promoted *TREX2* mRNA and protein expression, but not *TREX1* mRNA and protein expression (Figure S5D–S5K). Collectively, glucose acts through NSUN2 binding to maintain m^5C RNA methylation and mRNA stability of *TREX2*.

We then determined whether TREX2 displays oncogenic activity and is responsible for the oncogenic activity of the glucose/NSUN2 axis. TREX2 knockdown impaired cancer cell proliferation, survival, and cancer stemness (Figure S5L–S5P), whereas TREX2 overexpression promoted these oncogenic properties (Figure 4P–4T; Figure S5Q). While glucose restoration protected cancer cells from cell death upon glucose deprivation, loss of NSUN2 or TREX2 abrogated protection effect of glucose (Figure 4S; Figure S5P). Notably, restoration of TREX2 rescued, not only cell death from glucose deprivation or NSUN2 loss (Figure 4S), but also the defects in cancer cell proliferation, survival, and cancer stemness upon NSUN2 knockdown (Figure 4Q–4S; Figure S5Q). In a xenograft assay, overexpression of TREX2 promoted tumorigenesis, and restoration of TREX2 rescued the defect in tumorigenicity potential upon NSUN2 loss (Figure 4T). Collectively, these data underscore the importance of TREX2 in mediating oncogenic activity of the glucose/NSUN2 axis.

The Glucose/NSUN2/TREX2 Axis Restricts Cytosolic dsDNA Accumulation for cGAS/STING Activation to Maintain Oncogenic Activity of Cancer Cells

Although TREX2 is closely related to TREX1, which is involved in cGAS/STING repression by removing cytosolic ssDNA and dsDNA, its functional role in cGAS/STING signaling and cancer regulation remain puzzling. Accumulating evidence revealed that cGAS/STING pathway not only activates innate immunity for T cell activation, but also serves as a tumor suppressive signal by inducing apoptosis and cellular senescence in a cell autonomous manner [41]. Since TREX2 serves a key player responsible for oncogenic activity of the glucose/NSUN2 axis, we determined whether TREX2 impacts cGAS/STING activation to maintain oncogenic activity of the glucose/NSUN2/TREX2 axis. Similar to TREX1 deficiency [36–39] (Figure S6A), loss of TREX2 also triggered spontaneous activation of the cGAS/STING pathway, as determined by elevated 2′3′-cGAMP (cGAMP) for cGAS activation, phospho-STING (p-STING), phosphor-TBK1 (p-TBK1), phospho-IRF3 (p-IRF3), type I interferon-β (IFN-β) production and IFN response gene (*LGALS9*) expression [42] without changes in cGAS protein level, accompanied by elevated caspase-3 activation indicative of apoptosis (Figure S6B–S6G). Like TREX2 loss, glucose deprivation and NSUN2 loss also elevated cGAMP, p-STING, p-TBK1, p-IRF3, IFN-β production, IFN response gene (*LGALS9*) expression and caspase-3 activation without changing cGAS protein level (Figure 5A and 5B; Figure S6H–S6Y), which could be reversed by glucose and NSUN2, respectively, but not the NSUN2 mutant (Δ aa 1–28) (Figure 5B and 5C). Remarkably, loss of NSUN2 impaired the suppressive effect of glucose on p-STING, p-TBK1, p-IRF3, IFN-β production and caspase-3 activation (Figure 5A and 5B; Figure S6W and S6X).

Notably, adding 2DG and 3OMG, but not G6P, rescued TREX2 expression and repressed cGAS/STING and caspase-3 activation in cell-based assays under glucose starvation (Figure S6L–S6N). Furthermore, blocking the glucose/NSUN2 interaction by the TAT-N28 peptide also enhanced the levels of p-STING, p-TBK1, p-IRF3, IFN-β production and caspase-3 activation and compromised glucose's suppressive effects (Figure 5D and 5E), accompanied by reduced TREX2 protein level (Figure 4K). Remarkably, elevated cGAMP, p-STING, p-TBK1, p-IRF3, IFN-β production and caspase-3 activation upon NSUN2 loss was rescued

by TREX2 restoration (Figure 5F and 5G; Figure S6Z). While glucose, NSUN2 or TREX2 overexpression suppressed the levels of p-STING, p-TBK1 and p-IRF3, IFN-β production and caspase-3 activation (Figure S7A–S7D), the suppressive effects of glucose could be reversed by TREX2 knockdown or by adding cGAMP (Figure 5H and 5I; Figure S7E). Notably, elevated p-STING, p-TBK1 and p-IRF3, IFN-β production and caspase-3 activation upon glucose deprivation or NSUN2 loss could be reversed upon loss of STING or cGAS (Figure 5J and 5K; Figure S7F–S7J). A previous study showed that AMPK can regulate innate immunity through directly phosphorylating TBK1 [43]. We ruled out the involvement of AMPK in cGAS/STING activation upon glucose deprivation, since AMPK inactivation by its inhibitor compound C or AMPK deficiency failed to compromise cGAS/STING activation induced by glucose deprivation (Figure S7K and S7L). Collectively, the glucose/NSUN2/TREX2 axis serves as a key repressor to restrict cGAS/STING activation.

Cytosolic dsDNA accumulation is known to drive activation of cGAS/STING pathway [44]. Strikingly, glucose deprivation triggered spontaneous cytosolic dsDNA accumulation, which was reversed by adding back glucose (Figure 5L and 5M; Figure S8A–S8D). Interestingly, the accumulation of cytosolic DNA consisted of both cytosolic ssDNA and dsDNA upon glucose deprivation (Fig. S8A–S8D). Similar to glucose deprivation, loss of NSUN2 or TREX2 also induced cytosolic dsDNA accumulation (Figure 5L and 5M; Figure S8E–S8J). We found that TREX2 is localized both in the nucleus and cytosol (Figure S9A and S9B). Notably, restoration of NSUN2, but not the NSUN2 mutant (Δ aa 1–28), rescued cytosolic dsDNA accumulation in NSUN2 knockdown cancer cells (Figure S8E and S8F). While adding back glucose rescued spontaneous cytosolic dsDNA accumulation upon glucose deprivation, this effect was abolished by the TAT-N28 peptide, NSUN2 knockdown or TREX2 knockdown (Figure 5L–5O; Figure S8I and S8J; Figure S9C–S9F). Moreover, adding back TREX2 abrogated spontaneous cytosolic dsDNA accumulation upon glucose deprivation or NSUN2 knockdown (Figure S9G–S9J). We conclude that the glucose/NSUN2/TREX2 axis serves as a key mechanism to restrict cytosolic dsDNA accumulation.

TREX1 displays 3’ to 5’ exonuclease activity to remove cytosolic dsDNA [45]. To understand whether there is a redundant role of TREX1 and TREX2 in regulating cytosolic dsDNA levels, we generated TREX1 knockdown, TREX2 knockdown and TREX1/TREX2 double knockdown cells (Figure S5L; Figure S6A and S6C). Consistently, TREX1 knockdown caused the accumulation of cytosolic dsDNA, similar to TREX2 knockdown. However, both TREX1 and TREX2 knockdown did not further enhance cytosolic dsDNA levels compared with TREX1 knockdown or TREX2 knockdown (Figure S8G and S8H), suggesting that TREX1 and TREX2 play non-redundant roles in regulating cytosolic dsDNA levels. In light of these data, we speculated that TREX1 and TREX2 may work together to reduce cytosolic dsDNA levels, as a recent review indicated that TREX1 and TREX2 are functional dimers [34]. Future studies will be warranted to further understand why both TREX1 and TREX2 regulate cytosolic dsDNA levels.

TREX2 was shown to be associated with DNA repair processes in mouse ES cells [46]. To understand if spontaneous DNA damage occurs upon TREX2 knockdown, we examined the γH2AX levels using immunoblotting assay. γH2AX was only slightly induced upon TREX2

knockdown compared with control knockdown cancer cells, indicating that DNA damage response may not be induced by TREX2. While the low basal of γH2AX detected under glucose deprivation is inhibited by glucose, loss of TREX2 abrogated this suppressive effect by glucose (Figure S9K).

Since cGAS/STING serves as a tumor suppressing signal by inducing apoptosis, we next determined whether the oncogenic activity induced by the glucose/NSUN2/TREX2 axis may act through cGAS/STING repression. As expected, cGAS or STING knockdown reduced basal levels of p-STING, p-TBK1 and p-IRF3 and caspase-3 activation and promoted cancer cell proliferation, survival and cancer stemness (Figure S7F and S7G; Figure S9L–S9Q). Remarkably, cGAS or STING knockdown rescued the defects in cancer cell proliferation, survival and cancer stemness upon NSUN2 knockdown (Figure 5P–5S). Moreover, cGAS or STING knockdown also rescued the defect in cell survival upon glucose deprivation (Figure 5S). In a xenograft assay, cGAS knockdown or STING knockdown also rescued the defect in tumorigenesis upon NSUN2 loss (Figure 5T). Collectively, glucose/NSUN2/TREX2 maintains oncogenic properties by restricting cGAS/STING activation.

The Glucose/NSUN2/TREX2 Axis Drives Anti-PD-L1 Immunotherapy Resistance through Restricting cGAS/STING Signaling

cGAS/STING signaling activation plays a critical role in maintaining the efficacy of anti-PD-1/anti-PD-L1 immunotherapy in cancer suppression [47–50]. As the glucose/NSUN2/TREX2 axis restricts cGAS/STING activation, we asked whether aberrant activation of glucose/NSUN2/TREX2 drives the resistance of cancer cells to anti-PD-L1 immunotherapy. To address this question, we overexpressed vectors of NSUN2 or the NSUN2 mutant (Δ aa 1–28) in B16 melanoma cells and CT26 colon cancer cells, both of which are sensitive to anti-PD-L1 immunotherapy [51–53]. As expected, NSUN2, but not the NSUN2 mutant (Δ aa 1–28), induced TREX2 expression and led to cGAS/STING signaling suppression (Figure S10A and S10B). In B16 syngeneic tumor model with intact immunity, NSUN2, but not the NSUN2 mutant (Δ aa 1–28), promoted tumorigenesis and caused the resistance of B16 tumor to anti-PD-L1 immunotherapy (Figure 6A and 6B). Similar results were also obtained in CT26 tumor model (Figure 6C and 6D). Of note, loss of TREX2 abolished the tumor promotive effect and resistance to anti-PD-L1 immunotherapy induced by NSUN2 overexpression (Figure 6E and 6F; Figure S10C–S10F). In the tumor sections, overexpression of NSUN2, but not the NSUN2 mutant (Δ aa 1–28), reduced cGAS/STING signaling, as determined by reduced p-STING, p-TBK1 and p-IRF3 levels, caspase-3 activation indicative of apoptosis, $CD3^+$ and $CD8^+$ T cell infiltration upon anti-PD-L1 immunotherapy treatment (Figure 6G–6L, Figure S10G). Thus, the glucose/NSUN2/TREX2 axis drives cGAS/STING signaling repression and anti-PD-L1 immunotherapy resistance by restricting apoptosis and $CD8^+$ T cell infiltration.

To understand whether genetically targeting the glucose/NSUN2/TREX2 axis is a promising strategy to overcome anti-PD-L1 immunotherapy resistance in those cold tumors, we knocked down NSUN2 or TREX2 in 4T1 breast cancer cells and TRAMP-C2 prostate cancer cells, which are unresponsive to anti-PD-L1 immunotherapy [54,55]. Expectedly, NSUN2 loss and TREX2 loss in these two cancer cell lines also induced cGAS/

STING signaling activation (Figure S11A–S11D). Remarkably, NSUN2 or TREX2 loss could reduce tumorigenesis and overcome anti-PD-L1 immunotherapy resistance in these syngeneic tumor models (Figure 7A–7D). However, STING loss restored the tumorigenesis and abolished the reversal effect of anti-PD-L1 immunotherapy resistance upon NSUN2 or TREX2 deficiency (Figure 7A–7D; Figure S11E–S11J). In the tumor sections, NSUN2 or TREX2 loss induced cGAS/STING signaling, caspase-3 activation, and $CD3^+$ and $CD8^+$ T cell infiltration in response to anti-PD-L1 immunotherapy, which were impaired upon STING loss (Figure 7E–7G; Figure S11K–S11N). Collectively, our data provide proof-of-principle evidence that targeting the glucose/NSUN2/TREX2 axis can suppress tumorigenesis and overcome anti-PD-L1 immunotherapy resistance in those cold tumors through cGAS/STING activation for apoptosis and $CD8^+$ T cell infiltration.

DISCUSSION

Our study reveals an unprecedented finding that glucose serves as a signaling molecule that directly binds to NSUN2 at aa 1–28, leading to NSUN2 oligomerization and activation to maintain global m^5C RNA methylation independently of glucose metabolism. Notably, the glucose/NSUN2 axis elicits m^5C RNA methylation of *TREX2* and stabilizes *TREX2* mRNA for enhanced protein expression to maintain oncogenic properties and tumorigenesis. Strikingly, disrupting glucose/NSUN2 binding by the TAT-N28 peptide impairs NSUN2 activity, TREX2 expression and subsequent oncogenic processes, offering a potential strategy to target cancer without impacting normal glucose metabolism. Our study therefore identifies NSUN2 as a glucose sensor whose activation by glucose drives TREX2 expression to maintain tumorigenesis, defining the first mechanistic insight into how NSUN2 is activated by a nutrient. Thus, glucose serves as a cofactor for NSUN2 methyltransferase activation, extending the earlier findings that α-ketoglutarate serves as a cofactor for histone demethylase activation [56,57].

The cGAS/STING pathway has emerged to play a key role in both cancer immunity and intrinsic tumor suppression. Our study identifies the glucose/NSUN2/TREX2 axis as a key pathway to repress dsDNA accumulation and subsequent cGAS/STING activation leading to promoting oncogenic processes. Notably, glucose deprivation or NSUN2 loss leads to spontaneous dsDNA accumulation and cGAS/STING activation, which can be reversed by TREX2 restoration. Our study therefore places TREX2 exonuclease as a key downstream effector of glucose/NSUN2 in preventing dsDNA accumulation and cGAS/STING activation. Of note is that the glucose/NSUN2/TREX2 axis serves a key mechanism to drive anti-PD-L1 immunotherapy resistance through cGAS/STING repression for apoptosis and subsequent impairment of $CD8^+$ T cell infiltration, whereas genetic deletion of this axis overcomes anti-PD-L1 immunotherapy resistance through cGAS/STING signaling activation in syngeneic tumor models. Hence, targeting the glucose/NSUN2/TREX2 axis provides a promising strategy to elicit cGAS/STING activation leading to apoptosis and $CD8^+$ T cell infiltration and overcoming immunotherapy resistance in those cold tumors such as prostate cancer that are refractory to immunotherapy [58].

In summary, our study provides the compelling evidence that glucose can serve as a signaling molecule that directly binds to and activates NSUN2 to maintain m^5C RNA

methylation and mRNA stability of *TREX2*, resulting in cGAS/STING repression to shut off interferon response and promote oncogenic processes and immunotherapy resistance (Figure 7H), thus opening a new avenue for studying glucose's novel actions as a signaling molecule in regulating diverse biological processes. Our study not only provides new insights into how glucose elicits its oncogenic activity, but also offers novel paradigms and strategies for targeting cancers with aberrant glucose signaling. We also note that during the course of our paper revision, a recent study revealed that glucose could also bind directly to DDX21 and caused the dissociation of DDX21 leading to the regulation of mRNA splicing and tissue differentiation [19]. It will be important to further explore additional glucose sensors mediating glucose's actions on regulating diverse biological processes for cancer and disease progression.

Limitations of Study

While our study has demonstrated the key role of the glucose/NSUN2/TREX2 axis in driving anti-PD-L1 immunotherapy resistance at least in part through cGAS/STING repression using various syngenieic mouse tumor models, it will be necessary to validate this notion further using patient-derived xenografts (PDXs) grown in humanized mice with intact immunity. It will also be important to explore whether targeting the glucose/NSUN2 axis by the TAT-N28 peptide is sufficient to overcome anti-PD-L1 immunotherapy resistance in these PDX models.

STAR ★ METHODS

RESOURCE AVAILABILITY

Lead contact—Further information and requests for resources and reagents may be directed to and will be fulfilled by the Lead Contact, Hui-Kuan Lin (hui-kuan.lin@duke.edu).

Materials availability—All the materials generated and used in this study will be available upon request.

Data and code availability

- Uncropped scans of all blots and all values used to generate graphs are included in Data S1 - Source Data, which has been deposited at Mendeley and are publicly available as of the date of publication. The DOI is listed in the Key Resources Table.
- This paper does not report original code.
- Any additional information required to reanalyze the data reported in this paper is available from the lead contact upon request.

EXPERIMENTAL MODEL AND STUDY PARTICIPANT DETAILS

Animal studies—Animals were housed in a specific-pathogen-free facility under standard conditions. The animal protocol was approved by Institutional Animal Care and Use Committee at Wake Forest University School of Medicine. All mice (6-week-old) were

purchased from Charles River Laboratories (n = 5 for each group). For *in vivo* xenograft tumorigenesis assays, Hep3B or PC3 cells (1×10^6) were injected subcutaneously (s.c.) into athymic nude mice (Crl:NU(NCr)-Foxn1^{nu}, Code 490, male). In syngeneic mouse model (allograft) study, B16 or TRAMP-C2 cells (5×10^5) were injected s.c. into C57BL/6 (Code 027, male) mice; CT26 (5×10^5) or 4T1 cells (1×10^4) were injected s.c. into BALB/c (NCI BALB-cAnNCr, Code 555, female) mice. The dose and dosing schedule used with anti-mouse PD-L1 (Clone 10F.9G2) or rat IgG2b isotype control antibodies was 100 or 200 μg per intra-peritoneally administered at 3-to-5-day intervals. Tumor was measured by Caliper for length and width, and tumor volume was determined based on the formula: V = (Length x Width x Width)/2.

Cell culture—Hep3B, HEK293, HEK293T, PC3, B16, CT26, 4T1, TRAMP-C2, AMPK$^{-/-}$ MEF were cultured in required medium supplied with 10% Fetal Bovine Serum (FBS) and 1% Penicillin/Streptomycin at 37 °C under 5 % CO_2.

METHOD DETAILS

The synthesis of biotin-glucose—

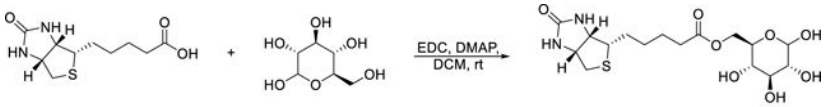

Biotin Glucose Biotin-glucose

A suspension of 180 mg of glucose (1 mM), 384 mg of 1-ethyl-3-(3-dimethylaminopropyl) carbodiimide hydrochloride (EDC) (2 mM) and 11 mg of 4-dimethylaminopyridine (DMAP) (0.01 mM) in dichloromethane (DCM) (5 mL) was stirred at room temperature (RT). 244 mg of biotin (1 mM) in 5 mL of DCM was added and the reaction mixture was stirred continually overnight. The solvent was removed, and the final compound were purified by silica gel column chromatography using a gradient of methanol/dichloromethane (0–10%). 230 mg of wax solid is obtained, and the yield was 57%. LCMS (ESI) m/z calcd for C16H27N2O8S+ (M+H)+ 407, found 407.

Synthesis of biotin-labeled 2-deoxy-D-glucose—

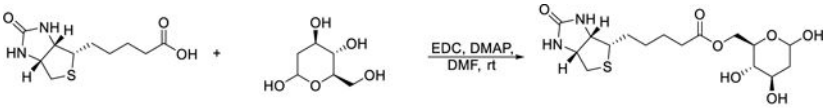

Biotin 2-deoxy-D-glucose (2-DG) Biotin-2-DG

A solution of 328 mg of 2-deoxy-D-glucose (2DG, 2 mM), 768 mg of EDC (4 mM) and 22 mg of DMAP (0.02 mM) in dry N, N-dimethylformamide (DMF) (5 mL) was stirred at RT. 488 mg of biotin (2 mM) in dry DMF (5 mL) was added and the reaction mixture was stirred at RT overnight. Then the reaction mixture was concentrated under vacuum to remove DMF to afford a light-yellow wax. The wax was washed with 10.0 mL DCM and the solid was collected and dried under vacuum to afford 494 mg of light-yellow foam as the crude product of biotin-2DG with yield 50.5%. LCMS (ESI) m/z calcd for C16H26N2O7S+ (M+H)+ 390, found 391.

Glucose starvation and restoration—For glucose deprivation, cells were washed with PBS for twice and cultured in glucose-free DMEM supplied with dialyzed FBS for indicated time. The cells were stimulated by the addition of DMEM with glucose, 2DG, 3OMG, G6P, peptide, or cGAMP for 2h.

Plasmid constructions—Full-length CDSs of human *NSUN2* genes (GeneID: 54888; F1: NM_017755.6, transcript variant 1; F2: NM_001193455.2, transcript variant 2; F3: NR_037947.2, transcript variant 3) were amplified by PCR using human HEK293 cDNA and subcloned into pGEX-6P-1. The human *NSUN2* mutants were generated based on the full-length *NSUN2*-F1 expression vector with Q5 Site-Directed Mutagenesis Kit (New England Biolabs) according to the manufacturer's instructions. The corresponding primers used are as followed: *NSUN2*-F1 (forward, 5′-CGGAATTCATGGGGCGGCGTTCGCGGG-3′; reverse, 5′-CCGCTCGAGTTACCGGGGTGGATGGACC-3′), *NSUN2*-F2 (forward, 5′-CGGAATTCATGGGGCGGCGTTCGCGGG-3′; reverse, 5′-CCGCTCGAGTTACCGGGGTGGATGGACC-3′), *NSUN2*-F3 (forward, 5′-CGGAATTCATGGTGGTCAATCACGATGCC-3′; reverse, 5′-CCGCTCGAGTTACCGGGGTGGATGGACC-3′), *NSUN2*-Δ1–84 (forward, 5′-GGATCCCCGGAATTCAGCCACGCAAAAGAG −3′; reverse, 5′- CTCTTTTGCGTGGCTGAATTCCGGGGATCC-3′), *NSUN2*-Δ184–190 (forward, 5′-AAGATCTTAGATATGACCACACAGTTAATT −3′; reverse, 5′- AATTAACTGTGTGGTCATATCTAAGATCTT-3′), *NSUN2*-Δ121–236 (forward, 5′-CAGCCACTGAGTTGGATGGTGGTCAACCAT-3′; reverse, 5′- ATGGTTGACCACCATCCAACTCAGTGGCTG-3′), *NSUN2*-Δ1–28 (forward, 5′-GGATCCCCGGAATTCCGCGGCGAGGCGGG −3′; reverse, 5′- GCCCGCCTCGCCGCGGAATTCCGGGGATCC-3′), *NSUN2*-Δ29–56 (forward, 5′-GAGGGTGGTGGAAAGATCGTGCCCGAGGGC −3′; reverse, 5′- GCCCTCGGGCACGATCTTTCCACCACCCTC-3′), *NSUN2*-Δ57–84 (forward, 5′-TACCAGGAGCTCAAGAGCCACGCAAAAGAG-3′; reverse, 5′-CTCTTTTGCGTGGCTCTTGAGCTCCTGGTA-3′). All plasmids were validated by DNA sequencing and prepared with the Fastfilter Plasmid Midi Kit (Omega Bio-tek).
To clone *NSUN2* or its mutant or *TREX2* into mammalian expressing vector, full-length CDSs of human *NSUN2*-F1 (NM_017755.6) or *TREX2* (NM_080701.4) were amplified by PCR using human HEK293 cDNA and subcloned into pFLAG-CMV2 vector (Sigma-Aldrich) or pCDH-blasticidin vector. The corresponding primers used are as follow: *NSUN2*-F1 forward, 5′-CGGAATTCAATGGGGCGGCGGTCGCGGGG-3′; reverse, 5′-TCCGGTACCTTACCGGGGTGGATGGACCC-3′. *TREX2* forward, 5′- GGGAATTCATGTCCGAAGCACCCCGGGC-3′; reverse, 5′-CCGCTCGAGTCAGGCCTCCAAGCTGGGG-3′.

Expression and purification of recombinant protein—For purifying recombinant NSUN2 expression, GST-tagged pGEX-6P-1 expression vectors encoding NSUN2-F1, NSUN2-F2, NSUN2-F3, NSUN2-Δ1–84, NSUN2-Δ184–190, NSUN2-Δ121–236, NSUN2-Δ1–28, NSUN2-Δ29–56, or NSUN2-Δ57–84 mutants were transformed into *Escherichia coli* BL21 (DE3). The cells were grown in LB (Lysogeny broth) medium at 37 °C. When the

culture reached an OD600 of 0.6, 1 mM IPTG was added. The culture was transferred to a shaking incubator at 20 °C for overnight. Recombinant proteins were then purified using Glutathione Sepharose® 4B and cleaved with PreScission protease according to the manufacturer's instructions. Recombinant proteins were subjected to SDS-PAGE, followed by Coomassie brilliant blue staining (CBB) and immunoblotting to examine the purity of the recombinant proteins. The purified proteins were split and stored at −80 °C.

Immunoblotting—For immunoblotting, whole cell lysates were prepared from the cells lysed with E1A buffer (50 mM HEPES, pH 7.6, 250 mM NaCl, 0.1% Nonidet P-40, 5 mM EDTA) supplemented with complete protease inhibitor cocktail (Roche, 04693132001). Cell lysates were subjected to SDS-PAGE and proteins were visualized by enhanced chemiluminescence according to the manufacturer's instructions (Millipore).

Biotin pull-down assay—Biotin-glucose pull-down assays were performed according to our previous studies [22,28]. In brief, magic Dynabeads MyOne Streptavidin T1 (Thermal Fisher) was pre-incubated with free biotin or biotin-labeled glucose for 30 min at RT, and then incubated with cell lysates, recombinant proteins or peptides rotated overnight at 4 °C. The beads were washed with PBS for 4 times and analyzed by immunoblotting.

Lentiviral infection for gene knockdown and restoration—Lentiviral infection was performed based on our earlier studies [59,60]. To generate lentivirus-producing cell lines, calcium phosphate was used to transfect with luciferase (shluc), target gene shRNA, virusGag-Pol packing vector (pPAX) and virus envelope glycoprotein expression vector (pMD.2G) in HEK293T cells. Supernatants containing virus particles were collected 48 h after transfection, filtered (0.45 μm), purified by centrifugation, and stored at −80 °C. Infections were carried out overnight by incubating cells with supernatants in the presence of 8 μg/mL Polybrene (Sigma-Aldrich). After viral infection, cells were selected by puromycin (3 μg/ml) for 7 days. The individual mission shRNAs kept in frozen bacterial glycerol were purchased from Sigma-Aldrich. For restoration of *NSUN2*-WT, *NSUN2*-Δ28, and *TREX2* in NSUN2 knockdown cells, HEK293T were co-transfected with pCDH-*NSUN2*-WT, *NSUN2*-Δ28, and *TREX2*-blasticidin and package plasmids (pPAX/pMD.2G). After 48 h, virus containing supernatants were harvested to infect NSUN2 knockdown cells. All stably transfected cells were selected by blasticidin (5 μg/ml) for 7 days.

Immunofluorescence and confocal microscopy—Cells grown on autoclaved coverslips were fixed with 4% paraformaldehyde (PFA) for 20 min and permeabilized with 0.4% Triton X-100 for 7 to 10 min and blocked with 5% BSA for 1 h. The primary antibody against dsDNA was applied onto the cells and incubated overnight at 4 °C. Cells then were washed with 1×PBS, incubated with a secondary antibody (Alexa 488 fluorescein-conjugated anti-mouse IgG) for 1 h at RT, and washed twice by 1×PBS. Coverslips were then mounted on a slide using one drop of mounting medium containing DAPI. The images were acquired using Olympus FV1200 Spectral Laser Scanning Confocal Microscope [61].

RNA isolation and m^{5}C Dot blot assay—Total RNA was extracted by using Quick-RNA™ Miniprep Kit (ZYMO Research) according to manufacturer's manual. RNA samples were quantified by 2200 Tape Station (Agilent). For Dot blot assay, equal amounts of RNA

were loaded onto the positive charged nylon transfer membrane (GE Healthcare). After UV crosslinking (Stratalinker® UV Crosslinker 1800) for 3 min at 254 nm, the membrane was blocked with 5% non-fat dried milk in PBS with 0.1% Tween-20 (PBST), followed by incubation with the primary rabbit anti-m^5C antibody (CST, 28692S) and then peroxidase affinipure goat anti-Rabbit IgG (H+L) (Jacksonimmuno, 111–035-003) secondary antibody. m^5C RNA levels were visualized by enhanced chemiluminescence (Millipore). Equal RNA loading was verified by methylene blue (MB, Sigma-Aldrich) staining. The intensity of Dot blot signal was quantified by ImageJ.

Quantitative real time polymerase chain reaction (RT-qPCR)—Total RNAs (0.5 to 1 μg) were subjected to reverse transcription with PrimeScript RT Master Mix (Takara, DRR036A). To determine relative mRNA level, RT-qPCR was performed using 2x SYBR Green qPCR Master Mix (BIMAKE, B21203) and gene expression was normalized with *GAPDH*. ΔΔCt method [62] was used to indicate the relative expression level of corresponding genes. Primers used for RT-qPCR were listed in Table S4.

In vitro *methylation assays*—To measure NSUN2 activity, the *in vitro* methylation assay by NSUN2 was performed as described previously [63]. Briefly, 50 μl of reaction mixture containing 0.2 nM purified NSUN2 proteins, 0.01 nM RNA, and 1 μCi of ^3H-labeled S-adenosyl-L-methionine ([^3H]SAM, ART 0288–250 μCi, American radiolabelled) in reaction buffer (5 mM Tris HCL [pH 7.5], 5 mM EDTA, 10% glycerol, 1.5 mM dithiothreitol, 5 mM $MgCl_2$) supplemented with inhibitors (leupeptin [1 μg/ml], aprotinin [1 μg/ml], 0.5 mM phenylmethylsulfonyl fluoride, and RNasin [5 U/ml, Promega]) was incubated for 45 min at 37 °C. Unincorporated [^3H]SAM in the reactions was removed by using Zymo-Spin IIICG Columns (ZYMO Research) and the incorporated radioactivity was measured by liquid scintillation counting.

Native-PAGE assay and chemical crosslinking—Protein samples were prepared with Native Sample Buffer and subjected to Native-PAGE, followed by immunoblotting. For chemical crosslinking, protein samples were proceeded with Bismaleimide Crosslinkers (BMH, Thermo) according to the manufacturer's instructions, followed by SDS-PAGE and immunoblotting.

Colony formation assay and apoptosis assay—For colony formation assay, cells (2×10^3) were plated into 12 well plates for 12 days. Cells were rinsed with PBS to remove the dead cells and stained with crystal violet, followed by incubating with 2% SDS. Absorption at 600 nm was measured to calculate the relative survival rate for each group. For apoptosis assay, cells were deprived with glucose for 22 h and then stimulated with DMEM medium with 5.5 mM glucose for 2 h. Then the cells were proceeded with the FITC Annexin V Staining Protocol (FITC Annexin V Apoptosis Detection Kit I, BD) to measure apoptosis.

Tumor sphere formation assay—For *in vitro* tumor sphere forming assay, 4×10^3 cells were seeded in the ultra-low attachment 6-well plate (Corning Life Science) and cultured in tumor sphere-forming medium (DME/F12 supplemented with 5 μg/ml insulin, 0.4% BSA, 20 ng/ml human epidermal growth factor, 10 ng/ml basic fibroblast growth factor, and 1 X

B-27™ Supplement [50X, Gibco]). Cells were incubated at 37 °C for 12 days and spheres larger than 50 μm were counted.

RNA-seq—Total RNA was isolated from shluc and sh*NSUN2* Hep3B cells, which were either glucose-starved for 6 h or glucose-starved for 4 h and then add-back glucose for 2 h, by using Quick-RNA™ Miniprep Kit (ZYMO Research) according to manufacturer's procedures. RNA samples were quantified by 2200 Tape Station (Agilent) and sent to GENEWIZ for RNA-seq using Illumina HiSeq 2×150 bp sequencing. Three independent biological replicates were performed for RNA-seq.

RNA-IP and gene-specific m^{5}C qPCR—RT-qPCR was performed to assess the relative abundance of the selected mRNA in m^{5}C antibody immunoprecipitation (IP) samples and input samples. Briefly, total RNA was isolated with Quick-RNA™ Miniprep Kit. 500 ng RNA was used as an input sample and the remaining RNA was used for m^{5}C IP. 100 μg of RNA was diluted into 500 μl IP buffer (150 mM NaCl, 0.1% NP-40, 10 mM Tris, pH 7.4, 100 U RNase inhibitor) and incubated with m^{5}C antibody at 4 °C for 2 h. Dynabeads® Protein A coated with BSA was added into the reaction solution and rotated for 2 h at 4 °C. After washing by IP buffer with RNase inhibitors four times, the m^{5}C IP portion was eluted with elution buffer (5 mM Tris-HCL [pH 7.5], 1 mM EDTA, 0.05% SDS, and 4 μl Proteinase K [20 mg/ml]). The final eluted mRNA was concentrated with a RNA Clean & Concentrator-5 kit. The same amounts of the concentrated IP RNA or input RNA from each sample were used for the cDNA library. The mRNA expression was determined by the number of amplification cycles (Cq). The relative m^{5}C levels in gene were calculated by the m^{5}C levels (m^{5}C IP) normalized with the expression of each gene from the input sample.

For mapping assay of the NSUN2 fragments binding to *TREX2* mRNA, similar to the procedure above RNA-IP were performed using anti-NSUN2 antibody along with various NSUN2 truncated proteins, followed by RT-qPCR analysis of *TREX2* mRNA.

RNA decay assay—Cells were seeded in 6-well plates and incubated overnight at 37 °C, treated with Actinomycin D (2 μg/ml, A1410, Sigma-Aldrich) for different time points, and harvested for the collection of RNA samples. *TREX2* mRNA levels against *GAPDH* RNA levels were analyzed by RT–qPCR. The half-life of *TREX2*, *ACTIN* and *NSUN2* mRNA normalized with *GAPDH* was then measured with their levels at t = 0 as 100% according to the previous study [64].

Enzyme-Linked Immunosorbent assay (ELISA)—To detect cGAMP levels in cells, treated cells were lysed in M-PER™ Mammalian Protein Extraction Reagent (Thermo Fisher) and the levels of cGAMP in cell lysates were measured by 2′ 3′-cGAMP competitive ELISA assay Kit (501700, Cayman) according to manufacturer's protocol and previous study [65]. To detect IFN-β levels in treated cells, cell culture media were centrifuged at 2,000 x g for 10 mins to remove debris and collected supernatants for assessing IFN-β levels by human IFN-β ELISA Kit (ab278127, Abcam) according to manufacturer's protocol.

Immunohistochemistry—Formalin-fixed, paraffin-embedded tumor tissue samples were sectioned at 4 μm. After deparaffinization and hydration, the sections were heated at 95 °C in citrate buffer (pH 6.0) for epitope retrieval, quenched with hydrogen peroxide blocking reagent to abolish endogenous peroxidase. To block nonspecific antibody binding, sections were incubated in blocking solution (10% normal goat serum in PBST) at RT for 1 h. Primary antibodies were incubated overnight at 4 °C. Secondary antibodies were incubated for 2 h at RT. The DAB Substrate Kit was used for visualization according to manufacturer's protocol. Finally, sections were counterstained with acid hematoxylin solution (12 min) and Scott's bluing reagent (5 min), dehydrated in an ascending alcohol series up to 100%, cleared with xylene (5 min), and coverslipped by Tissue-Tek Glas™ mounting medium.

QUANTIFICATION AND STATISTICAL ANALYSIS

All quantification were performed using ImageJ software. The schematic representations (Fig. 1A, 1D, 1F, 1H, 1J, and 4O) were created using PowerPoint. The heatmap (Fig. 4A) was created using Excel. The Graphical Abstracts and illustration of the mechanism (Fig. 7H) were created using BioRender. All the other graphs and Statistical Analysis were performed using GraphPad.Prism 7. Data were presented as mean ± SD. Statistical significance for pairwise comparison of variables were calculated using two-tailed unpaired Student's *t*-test. P values were calculated using a two-way ANOVA for cell growth curve, tumor volume changes and RNA decay assay. For all analyses, $p < 0.05$ were regarded as statistically significant. *, $p < 0.05$. **, $p < 0.01$. ***, $p < 0.001$. NS, non-significant. The 95% confidence intervals were used for all general statistical analyses. For mass spectrometry analysis and RNA-seq, samples were processed in random order and experimenters were blinded to experimental conditions. Data shown are representative of three independent experiments (biological replicates).

Supplementary Material

Refer to Web version on PubMed Central for supplementary material.

ACKNOWLEDGEMENTS

We acknowledge the support of the Wake Forest Baptist Comprehensive Cancer Center Cell & Cellular Imaging Shared of Resource and Flow cytometry Shared of Resource by the National Cancer Institute's Cancer Center Support Grant (P30CA012197). We thank Dr. Peiqing Sun for kindly providing the UV Crosslinker and Emily Lin for editing this manuscript. This work is supported in part by Start-ups from Wake Forest School of Medicine (H.K.L.), NIH grant (R01CA256158) (H.K.L.), and Anderson Endowed Professorship fund (H.K.L.).

REFERENCES

1. Bhattacharya B, Mohd Omar MF, and Soong R.(2016). The Warburg effect and drug resistance. Br J Pharmacol 173, 970–979. 10.1111/bph.13422. [PubMed: 26750865]
2. Dang CV (2012). Links between metabolism and cancer. Genes Dev 26, 877–890. 10.1101/gad.189365.112. [PubMed: 22549953]
3. Koppenol WH, Bounds PL, and Dang CV (2011). Otto Warburg's contributions to current concepts of cancer metabolism. Nat Rev Cancer 11, 325–337. 10.1038/nrc3038. [PubMed: 21508971]
4. Ward PS, and Thompson CB (2012). Metabolic reprogramming: a cancer hallmark even warburg did not anticipate. Cancer Cell 21, 297–308. 10.1016/j.ccr.2012.02.014. [PubMed: 22439925]

5. Szablewski L.(2013). Expression of glucose transporters in cancers. Biochim Biophys Acta 1835, 164–169. 10.1016/j.bbcan.2012.12.004. [PubMed: 23266512]
6. Hay N.(2016). Reprogramming glucose metabolism in cancer: can it be exploited for cancer therapy? Nat Rev Cancer 16, 635–649. 10.1038/nrc.2016.77. [PubMed: 27634447]
7. Cairns RA, Harris IS, and Mak TW (2011). Regulation of cancer cell metabolism. Nat Rev Cancer 11, 85–95. 10.1038/nrc2981. [PubMed: 21258394]
8. Lee AS (2014). Glucose-regulated proteins in cancer: molecular mechanisms and therapeutic potential. Nat Rev Cancer 14, 263–276. 10.1038/nrc3701. [PubMed: 24658275]
9. Friis RM, Wu BP, Reinke SN, Hockman DJ, Sykes BD, and Schultz MC (2009). A glycolytic burst drives glucose induction of global histone acetylation by picNuA4 and SAGA. Nucleic Acids Res 37, 3969–3980. 10.1093/nar/gkp270. [PubMed: 19406923]
10. Ladurner AG (2009). Chromatin places metabolism center stage. Cell 138, 18–20. 10.1016/j.cell.2009.06.025. [PubMed: 19596230]
11. Rathmell JC, and Newgard CB (2009). Biochemistry. A glucose-to-gene link. Science 324, 1021–1022. 10.1126/science.1174665. [PubMed: 19460991]
12. Wellen KE, Hatzivassiliou G, Sachdeva UM, Bui TV, Cross JR, and Thompson CB (2009). ATP-citrate lyase links cellular metabolism to histone acetylation. Science 324, 1076–1080. 10.1126/science.1164097. [PubMed: 19461003]
13. Zhang X, Li B, Rezaeian AH, Xu X, Chou PC, Jin G, Han F, Pan BS, Wang CY, Long J, et al. (2017). H3 ubiquitination by NEDD4 regulates H3 acetylation and tumorigenesis. Nat Commun 8, 14799. 10.1038/ncomms14799. [PubMed: 28300060]
14. Bandyopadhyay G, Sajan MP, Kanoh Y, Standaert ML, Burke TR Jr., Quon MJ, Reed BC, Dikic I, Noel LE, Newgard CB, and Farese R.(2000). Glucose activates mitogen-activated protein kinase (extracellular signal-regulated kinase) through proline-rich tyrosine kinase-2 and the Glut1 glucose transporter. J Biol Chem 275, 40817–40826. 10.1074/jbc.M007920200. [PubMed: 11007796]
15. Chellamuthu A, and Gray SG (2020). The RNA Methyltransferase NSUN2 and Its Potential Roles in Cancer. Cells 9. 10.3390/cells9081758.
16. Chen X, Li A, Sun BF, Yang Y, Han YN, Yuan X, Chen RX, Wei WS, Liu Y, Gao CC, et al. (2019). 5-methylcytosine promotes pathogenesis of bladder cancer through stabilizing mRNAs. Nat Cell Biol 21, 978–990. 10.1038/s41556-019-0361-y. [PubMed: 31358969]
17. Hu Y, Chen C, Tong X, Chen S, Hu X, Pan B, Sun X, Chen Z, Shi X, Hu Y, et al. (2021). NSUN2 modified by SUMO-2/3 promotes gastric cancer progression and regulates mRNA m5C methylation. Cell Death Dis 12, 842. 10.1038/s41419-021-04127-3. [PubMed: 34504059]
18. Mei L, Shen C, Miao R, Wang JZ, Cao MD, Zhang YS, Shi LH, Zhao GH, Wang MH, Wu LS, and Wei JF (2020). RNA methyltransferase NSUN2 promotes gastric cancer cell proliferation by repressing p57(Kip2) by an m(5)C-dependent manner. Cell Death Dis 11, 270. 10.1038/s41419-020-2487-z. [PubMed: 32332707]
19. Miao W, Porter DF, Lopez-Pajares V, Siprashvili Z, Meyers RM, Bai Y, Nguyen DT, Ko LA, Zarnegar BJ, Ferguson ID, et al. (2023). Glucose dissociates DDX21 dimers to regulate mRNA splicing and tissue differentiation. Cell 186, 80–97 e26. 10.1016/j.cell.2022.12.004. [PubMed: 36608661]
20. Ota T, Suzuki Y, Nishikawa T, Otsuki T, Sugiyama T, Irie R, Wakamatsu A, Hayashi K, Sato H, Nagai K, et al. (2004). Complete sequencing and characterization of 21,243 full-length human cDNAs. Nat Genet 36, 40–45. 10.1038/ng1285. [PubMed: 14702039]
21. Milletti F.(2012). Cell-penetrating peptides: classes, origin, and current landscape. Drug Discov Today 17, 850–860. 10.1016/j.drudis.2012.03.002. [PubMed: 22465171]
22. Zhang W, Wang G, Xu ZG, Tu H, Hu F, Dai J, Chang Y, Chen Y, Lu Y, Zeng H, et al. (2019). Lactate Is a Natural Suppressor of RLR Signaling by Targeting MAVS. Cell 178, 176–189 e115. 10.1016/j.cell.2019.05.003. [PubMed: 31155231]
23. Cheng JX, Chen L, Li Y, Cloe A, Yue M, Wei J, Watanabe KA, Shammo JM, Anastasi J, Shen QJ, et al. (2018). RNA cytosine methylation and methyltransferases mediate chromatin organization and 5-azacytidine response and resistance in leukaemia. Nat Commun 9, 1163. 10.1038/s41467-018-03513-4. [PubMed: 29563491]

24. Gkatza NA, Castro C, Harvey RF, Heiss M, Popis MC, Blanco S, Bornelov S, Sajini AA, Gleeson JG, Griffin JL, et al. (2019). Cytosine-5 RNA methylation links protein synthesis to cell metabolism. PLoS Biol 17, e3000297. 10.1371/journal.pbio.3000297.
25. Xie S, Chen W, Chen K, Chang Y, Yang F, Lin A, Shu Q, Zhou T, and Yan X.(2020). Emerging roles of RNA methylation in gastrointestinal cancers. Cancer Cell Int 20, 585. 10.1186/s12935-020-01679-w. [PubMed: 33372610]
26. Xue C, Zhao Y, and Li L.(2020). Advances in RNA cytosine-5 methylation: detection, regulatory mechanisms, biological functions and links to cancer. Biomark Res 8, 43. 10.1186/s40364-020-00225-0. [PubMed: 32944246]
27. Pajak B, Siwiak E, Soltyka M, Priebe A, Zielinski R, Fokt I, Ziemniak M, Jaskiewicz A, Borowski R, Domoradzki T, and Priebe W.(2019). 2-Deoxy-d-Glucose and Its Analogs: From Diagnostic to Therapeutic Agents. Int J Mol Sci 21. 10.3390/ijms21010234.
28. Hsu CC, Zhang X, Wang G, Zhang W, Cai Z, Pan BS, Gu H, Xu C, Jin G, Xu X, et al. (2021). Inositol serves as a natural inhibitor of mitochondrial fission by directly targeting AMPK. Mol Cell 81, 3803–3819 e3807. 10.1016/j.molcel.2021.08.025. [PubMed: 34547240]
29. Srivastava SS, Darling JE, Suryadi J, Morris JC, Drew ME, and Subramaniam S.(2020). Plasmodium vivax and human hexokinases share similar active sites but display distinct quaternary architectures. IUCrJ 7, 453–461. 10.1107/S2052252520002456.
30. Xie G, and Wilson JE (1990). Tetrameric structure of mitochondrially bound rat brain hexokinase: a crosslinking study. Arch Biochem Biophys 276, 285–293. 10.1016/0003-9861(90)90040-6. [PubMed: 2297228]
31. Hitosugi T, Kang S, Vander Heiden MG, Chung TW, Elf S, Lythgoe K, Dong S, Lonial S, Wang X, Chen GZ, et al. (2009). Tyrosine phosphorylation inhibits PKM2 to promote the Warburg effect and tumor growth. Sci Signal 2, ra73. 10.1126/scisignal.2000431.
32. Wang HJ, Hsieh YJ, Cheng WC, Lin CP, Lin YS, Yang SF, Chen CC, Izumiya Y, Yu JS, Kung HJ, and Wang WC (2014). JMJD5 regulates PKM2 nuclear translocation and reprograms HIF-1alpha-mediated glucose metabolism. Proc Natl Acad Sci U S A 111, 279–284. 10.1073/pnas.1311249111. [PubMed: 24344305]
33. Guo D, Tong Y, Jiang X, Meng Y, Jiang H, Du L, Wu Q, Li S, Luo S, Li M, et al. (2022). Aerobic glycolysis promotes tumor immune evasion by hexokinase2-mediated phosphorylation of IkappaBalpha. Cell Metab 34, 1312–1324 e1316. 10.1016/j.cmet.2022.08.002. [PubMed: 36007522]
34. Hemphill WO, and Perrino FW (2019). Measuring TREX1 and TREX2 exonuclease activities. Methods Enzymol 625, 109–133. 10.1016/bs.mie.2019.05.004. [PubMed: 31455522]
35. Mazur DJ, and Perrino FW (2001). Structure and expression of the TREX1 and TREX2 3’ --> 5’ exonuclease genes. J Biol Chem 276, 14718–14727. 10.1074/jbc.M010051200. [PubMed: 11278605]
36. Ablasser A, Hemmerling I, Schmid-Burgk JL, Behrendt R, Roers A, and Hornung V.(2014). TREX1 deficiency triggers cell-autonomous immunity in a cGAS-dependent manner. J Immunol 192, 5993–5997. 10.4049/jimmunol.1400737. [PubMed: 24813208]
37. Gao D, Li T, Li XD, Chen X, Li QZ, Wight-Carter M, and Chen ZJ (2015). Activation of cyclic GMP-AMP synthase by self-DNA causes autoimmune diseases. Proc Natl Acad Sci U S A 112, E5699–5705. 10.1073/pnas.1516465112. [PubMed: 26371324]
38. Hemphill WO, Simpson SR, Liu M, Salsbury FR Jr., Hollis T, Grayson JM, and Perrino FW (2021). TREX1 as a Novel Immunotherapeutic Target. Front Immunol 12, 660184. 10.3389/fimmu.2021.660184.
39. Vanpouille-Box C, Alard A, Aryankalayil MJ, Sarfraz Y, Diamond JM, Schneider RJ, Inghirami G, Coleman CN, Formenti SC, and Demaria S.(2017). DNA exonuclease Trex1 regulates radiotherapy-induced tumour immunogenicity. Nat Commun 8, 15618. 10.1038/ncomms15618. [PubMed: 28598415]
40. Sibbritt T, Patel HR, and Preiss T.(2013). Mapping and significance of the mRNA methylome. Wiley Interdiscip Rev RNA 4, 397–422. 10.1002/wrna.1166. [PubMed: 23681756]

41. Li T, and Chen ZJ (2018). The cGAS-cGAMP-STING pathway connects DNA damage to inflammation, senescence, and cancer. J Exp Med 215, 1287–1299. 10.1084/jem.20180139. [PubMed: 29622565]
42. Shaw AE, Hughes J, Gu Q, Behdenna A, Singer JB, Dennis T, Orton RJ, Varela M, Gifford RJ, Wilson SJ, and Palmarini M.(2017). Fundamental properties of the mammalian innate immune system revealed by multispecies comparison of type I interferon responses. PLoS Biol 15, e2004086. 10.1371/journal.pbio.2004086.
43. Zhang Q, Liu S, Zhang CS, Wu Q, Yu X, Zhou R, Meng F, Wang A, Zhang F, Chen S, et al. (2022). AMPK directly phosphorylates TBK1 to integrate glucose sensing into innate immunity. Mol Cell 82, 4519–4536 e4517. 10.1016/j.molcel.2022.10.026. [PubMed: 36384137]
44. Chen Q, Sun L, and Chen ZJ (2016). Regulation and function of the cGAS-STING pathway of cytosolic DNA sensing. Nat Immunol 17, 1142–1149. 10.1038/ni.3558. [PubMed: 27648547]
45. Grieves JL, Fye JM, Harvey S, Grayson JM, Hollis T, and Perrino FW (2015). Exonuclease TREX1 degrades double-stranded DNA to prevent spontaneous lupus-like inflammatory disease. Proc Natl Acad Sci U S A 112, 5117–5122. 10.1073/pnas.1423804112. [PubMed: 25848017]
46. Dumitrache LC, Hu L, and Hasty P.(2009). TREX2 exonuclease defective cells exhibit double-strand breaks and chromosomal fragments but not Robertsonian translocations. Mutat Res 662, 84–87. 10.1016/j.mrfmmm.2008.11.012. [PubMed: 19094998]
47. Ablasser A, and Chen ZJ (2019). cGAS in action: Expanding roles in immunity and inflammation. Science 363. 10.1126/science.aat8657.
48. Du H, Xu T, and Cui M.(2021). cGAS-STING signaling in cancer immunity and immunotherapy. Biomed Pharmacother 133, 110972. 10.1016/j.biopha.2020.110972. [PubMed: 33254021]
49. Fu J, Kanne DB, Leong M, Glickman LH, McWhirter SM, Lemmens E, Mechette K, Leong JJ, Lauer P, Liu W, et al. (2015). STING agonist formulated cancer vaccines can cure established tumors resistant to PD-1 blockade. Sci Transl Med 7, 283ra252. 10.1126/scitranslmed.aaa4306.
50. Wang H, Hu S, Chen X, Shi H, Chen C, Sun L, and Chen ZJ (2017). cGAS is essential for the antitumor effect of immune checkpoint blockade. Proc Natl Acad Sci U S A 114, 1637–1642. 10.1073/pnas.1621363114. [PubMed: 28137885]
51. Curran MA, Montalvo W, Yagita H, and Allison JP (2010). PD-1 and CTLA-4 combination blockade expands infiltrating T cells and reduces regulatory T and myeloid cells within B16 melanoma tumors. Proc Natl Acad Sci U S A 107, 4275–4280. 10.1073/pnas.0915174107. [PubMed: 20160101]
52. Pilon-Thomas S, Mackay A, Vohra N, and Mule JJ (2010). Blockade of programmed death ligand 1 enhances the therapeutic efficacy of combination immunotherapy against melanoma. J Immunol 184, 3442–3449. 10.4049/jimmunol.0904114. [PubMed: 20194714]
53. Sagiv-Barfi I, Kohrt HE, Czerwinski DK, Ng PP, Chang BY, and Levy R.(2015). Therapeutic antitumor immunity by checkpoint blockade is enhanced by ibrutinib, an inhibitor of both BTK and ITK. Proc Natl Acad Sci U S A 112, E966–972. 10.1073/pnas.1500712112. [PubMed: 25730880]
54. Chen W, Bamford RN, Edmondson EF, and Waldmann TA (2022). IL15 and Anti-PD-1 Augment the Efficacy of Agonistic Intratumoral Anti-CD40 in a Mouse Model with Multiple TRAMP-C2 Tumors. Clin Cancer Res 28, 2082–2093. 10.1158/1078-0432.CCR-21-0496. [PubMed: 35262675]
55. Oba T, Long MD, Keler T, Marsh HC, Minderman H, Abrams SI, Liu S, and Ito F.(2020). Overcoming primary and acquired resistance to anti-PD-L1 therapy by induction and activation of tumor-residing cDC1s. Nat Commun 11, 5415. 10.1038/s41467-020-19192-z. [PubMed: 33110069]
56. Klose RJ, Kallin EM, and Zhang Y.(2006). JmjC-domain-containing proteins and histone demethylation. Nat Rev Genet 7, 715–727. 10.1038/nrg1945. [PubMed: 16983801]
57. Tsukada Y, Fang J, Erdjument-Bromage H, Warren ME, Borchers CH, Tempst P, and Zhang Y.(2006). Histone demethylation by a family of JmjC domain-containing proteins. Nature 439, 811–816. 10.1038/nature04433. [PubMed: 16362057]
58. Venturini NJ, and Drake CG (2019). Immunotherapy for Prostate Cancer. Cold Spring Harb Perspect Med 9. 10.1101/cshperspect.a030627.

59. Chan CH, Li CF, Yang WL, Gao Y, Lee SW, Feng Z, Huang HY, Tsai KK, Flores LG, Shao Y, et al. (2012). The Skp2-SCF E3 ligase regulates Akt ubiquitination, glycolysis, herceptin sensitivity, and tumorigenesis. Cell 149, 1098–1111. 10.1016/j.cell.2012.02.065. [PubMed: 22632973]

60. Yang WL, Wang J, Chan CH, Lee SW, Campos AD, Lamothe B, Hur L, Grabiner BC, Lin X, Darnay BG, and Lin HK (2009). The E3 ligase TRAF6 regulates Akt ubiquitination and activation. Science 325, 1134–1138. 10.1126/science.1175065. [PubMed: 19713527]

61. Spada S, Yamazaki T, and Vanpouille-Box C.(2019). Detection and quantification of cytosolic DNA. Methods Enzymol 629, 17–33. 10.1016/bs.mie.2019.07.042. [PubMed: 31727239]

62. Livak KJ, and Schmittgen TD (2001). Analysis of relative gene expression data using real-time quantitative PCR and the 2(-Delta Delta C(T)) Method. Methods 25, 402–408. 10.1006/meth.2001.1262. [PubMed: 11846609]

63. Tang H, Fan X, Xing J, Liu Z, Jiang B, Dou Y, Gorospe M, and Wang W.(2015). NSun2 delays replicative senescence by repressing p27 (KIP1) translation and elevating CDK1 translation. Aging (Albany NY) 7, 1143–1158. 10.18632/aging.100860. [PubMed: 26687548]

64. Zhang X, Liu Z, Yi J, Tang H, Xing J, Yu M, Tong T, Shang Y, Gorospe M, and Wang W. (2012). The tRNA methyltransferase NSun2 stabilizes p16INK(4) mRNA by methylating the 3'-untranslated region of p16. Nat Commun 3, 712. 10.1038/ncomms1692. [PubMed: 22395603]

65. Yu CH, Davidson S, Harapas CR, Hilton JB, Mlodzianoski MJ, Laohamonthonkul P, Louis C, Low RRJ, Moecking J, De Nardo D, et al. (2020). TDP-43 Triggers Mitochondrial DNA Release via mPTP to Activate cGAS/STING in ALS. Cell 183, 636–649 e618. 10.1016/j.cell.2020.09.020. [PubMed: 33031745]

Highlights

- Glucose Promote Oligomerization and Activation of NSUN2 By Its Direct Binding to NSUN2
- The Glucose/NSUN2 Axis Maintains TREX2 Expression to Execute Its Oncogenic Activity
- The Axis represses cGAS/STING Activation to Maintain Oncogenic Activity of Cancer Cells
- The Axis Drives Anti-PD-L1 Immunotherapy Resistance By Restricting cGAS/STING Signaling

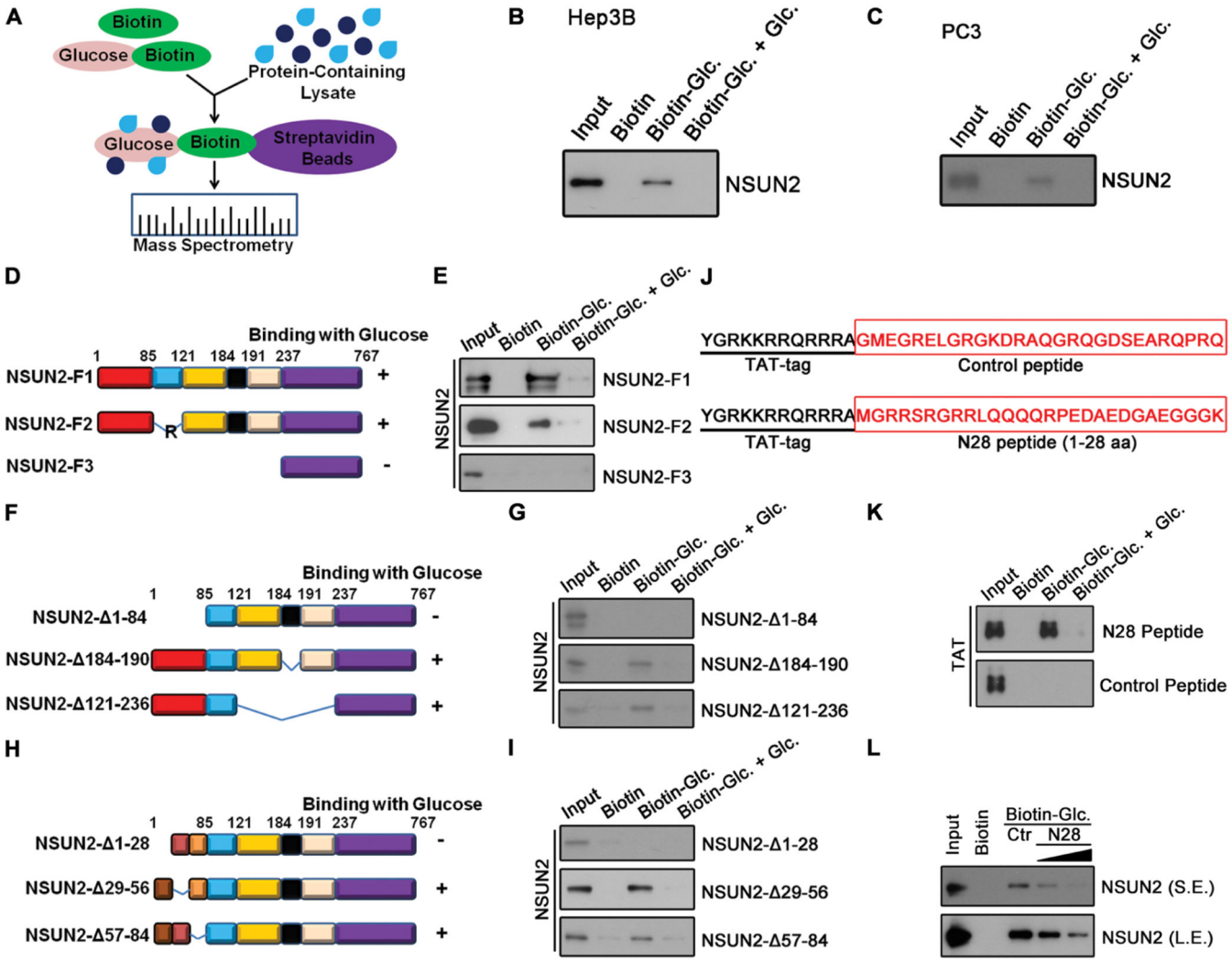

Figure 1. NSUN2 Is a Novel Interacting Protein of Glucose, and Its N-terminal Region Mediates Glucose Binding

(A) Identification of the potential glucose interacting proteins. Biotin or biotin-glucose was incubated with HEK293 cell lysate, followed by the incubation of streptavidin beads and subjected to mass spectrometry analysis (n = 3 biological replicates).

(B and C) Immunoblotting of binding complexes isolated from cell extracts of Hep3B (B) or PC3 (C) incubated with biotin or biotin-glucose (n = 3 biological replicates for each cell line).

(D) Schematic representations of three NSUN2 isoforms.

(E) Immunoblotting from *in vitro* mapping assays among biotin-glucose and NSUN2-F1, NSUN2-F2 or NSUN2-F3 proteins (n = 3 biological replicates).

(F) Schematic representations of various NSUN2 deletion mutants (NSUN2-Δ1–84, NSUN2-Δ184–190, NSUN2-Δ121–236).

(G) Immunoblotting from *in vitro* mapping assays among biotin-glucose and NSUN2-Δ1–84, NSUN2-Δ184–190, NSUN2-Δ121–236 proteins (n = 3 biological replicates).

(H) Schematic representations of various NSUN2 deletion mutants (NSUN2-Δ1–28, NSUN2-Δ29–56, NSUN2-Δ57–84).

(I) Immunoblotting from *in vitro* mapping assays among biotin-glucose and NSUN2-Δ1–28, NSUN2-Δ29–56, NSUN2-Δ57–84 proteins (n = 3 biological replicates).
(J) Schematic representations of the sequence for control or N28 peptide with a TAT tag in N-terminal region.
(K) Immunoblotting from *in vitro* pull-down assays by incubating biotin or biotin-glucose directly bind with control or N28 peptide (n = 3 biological replicates).
(L) Immunoblotting from *in vitro* pull-down assays by incubating biotin or biotin-glucose with NSUN2-F1 protein along with control or N28 peptide. S.E., short exposure; L.E., long exposure (n = 3 biological replicates).
See also Figure S1, Table S1 and Table S2.

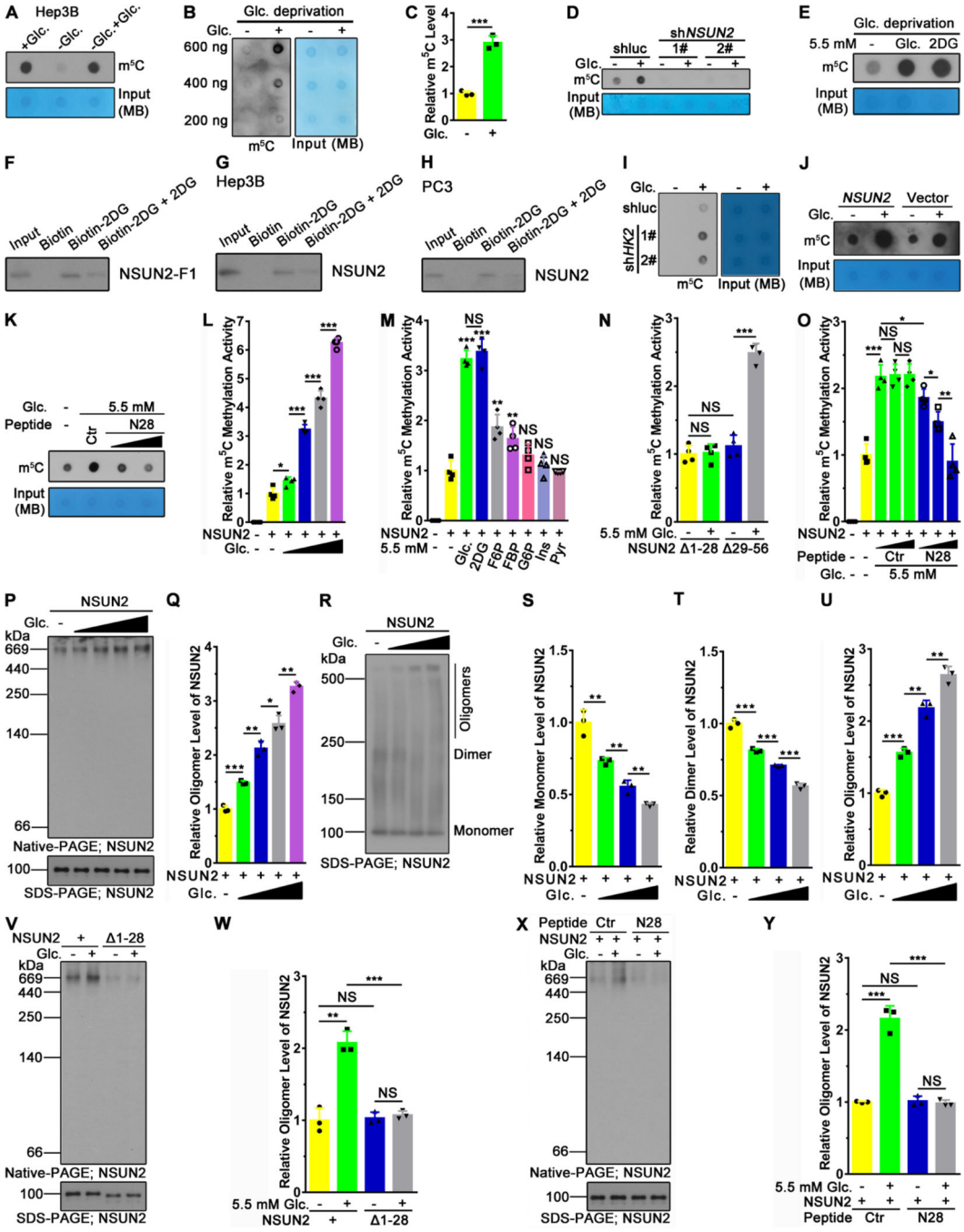

Figure 2. Glucose Serves As a Cofactor to Directly Promote Oligomerization and Activation of NSUN2

(A) Hep3B cells without or with glucose starvation for 4 h and restored with glucose (5.5 mM) 2 h before Dot blot assay of m^5C levels (total RNA) (n = 3 biological replicates).

(B) Hep3B cells were glucose-starved and restored with glucose, followed by Dot blot assay of m^5C levels (n = 3 biological replicates).

(C) The m^5C level intensity of (B) was determined using ImageJ (n = 3 biological replicates).

(D) NSUN2 knockdown Hep3B cells were glucose-starved for 4 h and restored with glucose (5.5 mM) 2 h for Dot blot assay (n = 3 biological replicates).
(E) Hep3B were glucose-starved for 4 h and restored with glucose or 2DG (5.5 mM) 2 h for Dot blot assay (n = 3 biological replicates).
(F) Immunoblotting from *in vitro* biotin pull-down assays among biotin-2DG and NSUN2-F1 protein (n = 3 biological replicates).
(G and H) Immunoblotting from cell extracts of Hep3B (G) or PC3 (H) incubated with biotin or biotin-2DG (n = 3 biological replicates for each cell line).
(I and J) HK2 knockdown (I) and NSUN2 overexpression (J) Hep3B cells were glucose-starved for 4 h and restored with glucose (5.5 mM) 2 h for Dot blot assay (n = 3 biological replicates).
(K) Hep3B cells were glucose-starved for 4 h and restored with glucose (5.5 mM) 2 h along with control (6 μM) or N28 (2 μM, 6 μM) peptide treatment for Dot blot assay (n = 3 biological replicates).
(L) *In vitro* m^5C RNA methylation assays for NSUN2 activity with various concentrations of glucose (2.75 mM, 5.5 mM, 11 mM, 25 mM) (n = 4 biological replicates).
(M) *In vitro* m^5C RNA methylation assays for NSUN2 activity with 2DG, glucose or its downstream metabolites (n = 4 biological replicates).
(N) *In vitro* m^5C RNA methylation assays using NSUN2-Δ1–28, NSUN2-Δ29–56 proteins along with or without glucose (n = 4 biological replicates).
(O) *In vitro* m^5C RNA methylation assays using NSUN2 protein along with control or N28 peptide (n = 4 biological replicates).
(P) Native-PAGE assay of NSUN2 protein with various concentrations of glucose (2.75 mM, 5.5 mM, 11 mM, 25 mM) (n = 3 biological replicates).
(Q) Quantification of relative oligomer level of NSUN2 in (P) by normalization with the total level of NSUN2 in SDS-PAGE (n = 3 biological replicates).
(R) Chemical crosslinking of NSUN2 protein with various concentrations of glucose (2.75 mM, 5.5 mM, 11 mM) (n = 3 biological replicates).
(S, T and U) Quantification of relative monomer (S), dimer (T), and oligomer (U) level of NSUN2 in (R) by normalization with the control group of no glucose (Lane 1) (n = 3 biological replicates).
(V and W) Native-PAGE assay (V) and quantification (W) of NSUN2, NSUN2-Δ1–28 proteins with or without glucose (5.5 mM).
(X and Y) Native-PAGE assay (X) and quantification (Y) NSUN2 protein along with control or N28 peptide, the relative level of NSUN2 oligomerization in Native-PAGE by normalization with the total level of NSUN2 in SDS-PAGE (n = 3 biological replicates).
Data are mean ± SD. *, $p < 0.05$, **, $p < 0.01$. ***, $p < 0.001$, NS, non-significant by Student's *t*-test (C, L-O, Q, S, T, U, W, Y). See also Figure S2.

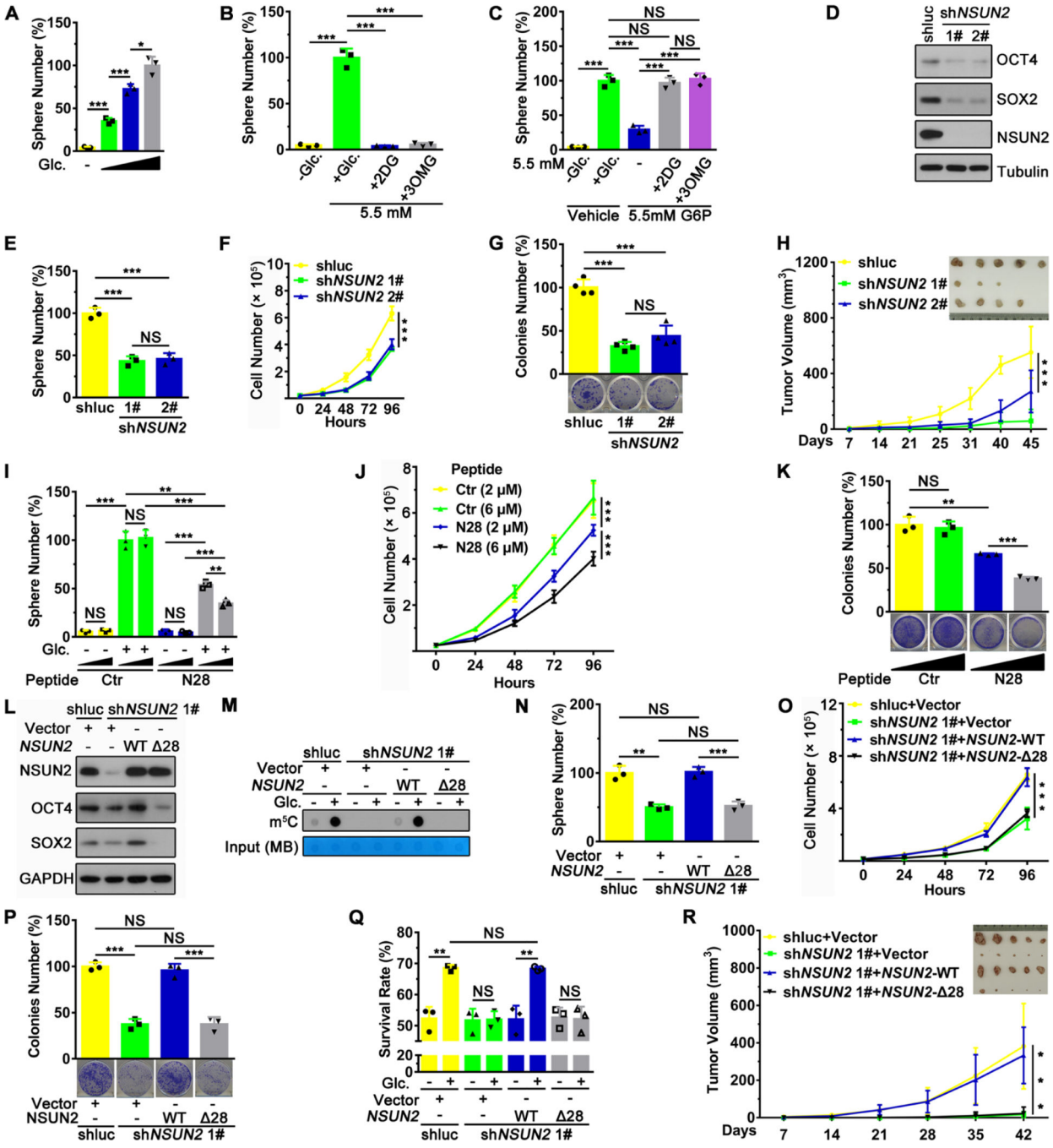

Figure 3. Glucose/NSUN2 Binding Leading to NSUN2 Activation Maintains Oncogenic Activity of Cancer Cells

(A) Sphere forming assays of Hep3B cells starved with glucose and restored with various concentrations of glucose (5.5 mM, 11 mM, 25 mM) (n = 3 biological replicates).

(B) Sphere forming assays of Hep3B cells treated with 0 mM glucose, 5.5 mM glucose, 5.5 mM 2DG or 5.5 mM 3OMG (n = 3 biological replicates).

(C) Sphere forming assays in glucose-starved Hep3B cells added back G6P (by transfection) with or without non-metabolizable glucose analog, 2DG or 3OMG (n = 3 biological replicates).

(D, E, F, and G) Control and NSUN2 knockdown Hep3B cells were subject to immunoblotting (D), sphere forming assays (E), growth curve (F) and colony forming assays (G) (n = 3 biological replicates).

(H) *In vivo* xenograft tumorigenesis assay of NSUN2 knockdown Hep3B cells subcutaneously injected to nude mice (n = 5 animals/group).

(I, J, and K) Hep3B cells incubated with control or N28 peptide (2 μM, 6 μM) were subjected to sphere forming assays (I), growth curve (J) and colony forming assays (K) (n = 3 biological replicates).

(L, M, N, O, P, and Q) Control and NSUN2 knockdown Hep3B cells restored with *NSUN2*-WT or *NSUN2*-Δ28 were subjected to immunoblotting (L), m^5C Dot blot assay (M), sphere forming assays (N), growth curve (O), colony forming assays (P) and survival rate (Q) (n = 3 biological replicates).

(R) *In vivo* xenograft tumorigenesis assay of control and NSUN2 knockdown Hep3B cells restored with *NSUN2*-WT or *NSUN2*-Δ28 subcutaneously injected to nude mice (n = 5 animals/group).

Data are mean ± SD. *, $p < 0.05$, **, $p < 0.01$, ***, $p < 0.001$, NS, non-significant by Student's *t*-test (A, B, C, E, G, I, K, N, P, Q) or by 2-way ANOVA (F, H, J, O, R). See also Figure S3.

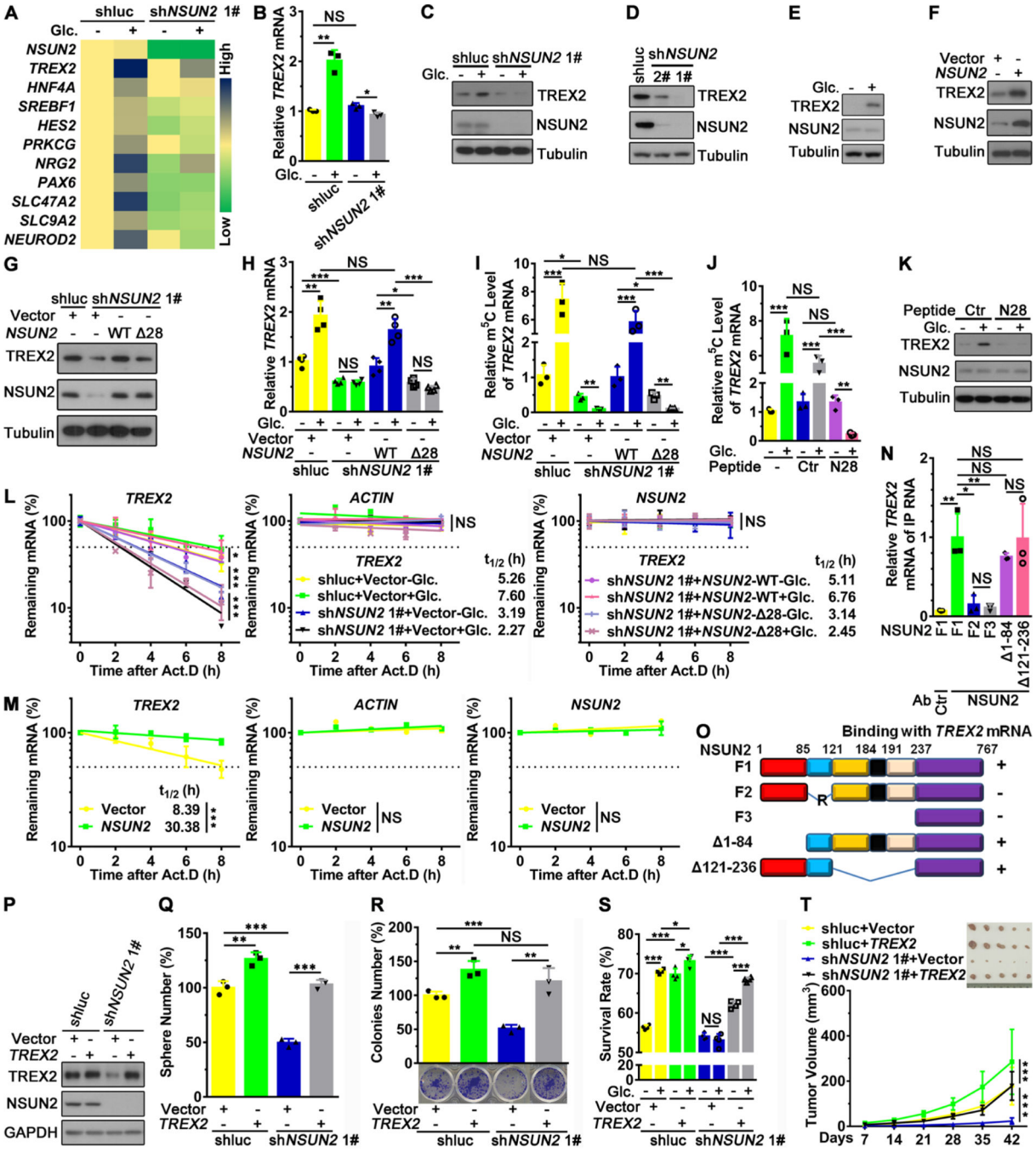

Figure 4. The Glucose/NSUN2 Axis Maintains TREX2 Expression to Execute Its Oncogenic Activity

(A) The heatmap for relative mRNA level of selected target genes from RNA-seq in NSUN2 knockdown Hep3B cells glucose-starved for 4 h and restored with glucose (5.5 mM) 2 h (n = 3 biological replicates).

(B and C) RT-qPCR analysis (B) and immunoblotting (C) in NSUN2 knockdown Hep3B cells glucose-starved for 4 h and restored with glucose (5.5 mM) 2 h (n = 3 biological replicates).

(D) Immunoblotting in NSUN2 knockdown Hep3B cells (n = 3 biological replicates).

(E) Immunoblotting in Hep3B cells glucose-starved for 4 h and restored with glucose (5.5 mM) 2 h (n = 3 biological replicates).
(F) Immunoblotting in NSUN2 overexpression Hep3B cells (n = 3 biological replicates).
(G) Immunoblotting in NSUN2 knockdown Hep3B cells restored with *NSUN2*-WT or *NSUN2*-Δ28 (n = 3 biological replicates).
(H) RT-qPCR analysis in the restoration of *NSUN2*-WT or *NSUN2*-Δ28 upon NSUN2 knockdown Hep3B cells with or without glucose (5.5 mM) (n = 3 biological replicates).
(I) RNA-IP using anti-m^5C antibody, followed by RT-qPCR analysis in the restoration of *NSUN2*-WT or *NSUN2*-Δ28 upon NSUN2 knockdown Hep3B cells with or without glucose (5.5 mM) (n = 3 biological replicates).
(J) RNA-IP using anti-m^5C antibody, followed by RT-qPCR analysis in Hep3B with glucose starvation for 4 h and restored with glucose (5.5 mM) 2 h along with control or N28 peptide treatment (n = 3 biological replicates).
(K) Immunoblotting in Hep3B cells, glucose-starved for 4 h and restored with glucose (5.5 mM) 2 h along with control or N28 peptide treatment (n = 3 biological replicates).
(L) RNA decay assay in the restoration of *NSUN2*-WT or *NSUN2*-Δ28 in NSUN2 knockdown Hep3B cells, glucose-starved and restored with glucose (n = 3 biological replicates).
(M) RNA decay assay in NSUN2 overexpression Hep3B cells treated with actinomycin D (Act. D, 2 μg/ml). RT-qPCR against *GAPDH* was performed to assess the half-life of *TREX2* and *ACTIN* mRNA (n = 3 biological replicates).
(N) RNA-IP using anti-NSUN2 antibody along with various NSUN2 truncated proteins, followed by RT-qPCR analysis of *TREX2* mRNA (n = 3 biological replicates).
(O) Schematic representations of mapping assay for the NSUN2 fragment binding to *TREX2* mRNA.
(P, Q, R, and S) Restoration of *TREX2* in NSUN2 knockdown Hep3B cells were subjected to immunoblotting (P), sphere forming assays (Q), colony forming assay (R), and survival rate (S) (n = 3 biological replicates).
(T) *In vivo* xenograft tumorigenesis assay of the restoration of *TREX2* in NSUN2 knockdown Hep3B subcutaneously inoculated in nude mice (n = 5 animals/group).
Data are mean ± SD. *, $p < 0.05$, **, $p < 0.01$, ***, $p < 0.001$, NS, non-significant by Student's *t*-test (A, B, H-J, N, Q-S) or by 2-way ANOVA (L, M, T). See also Figure S4 and S5, and Table S3.

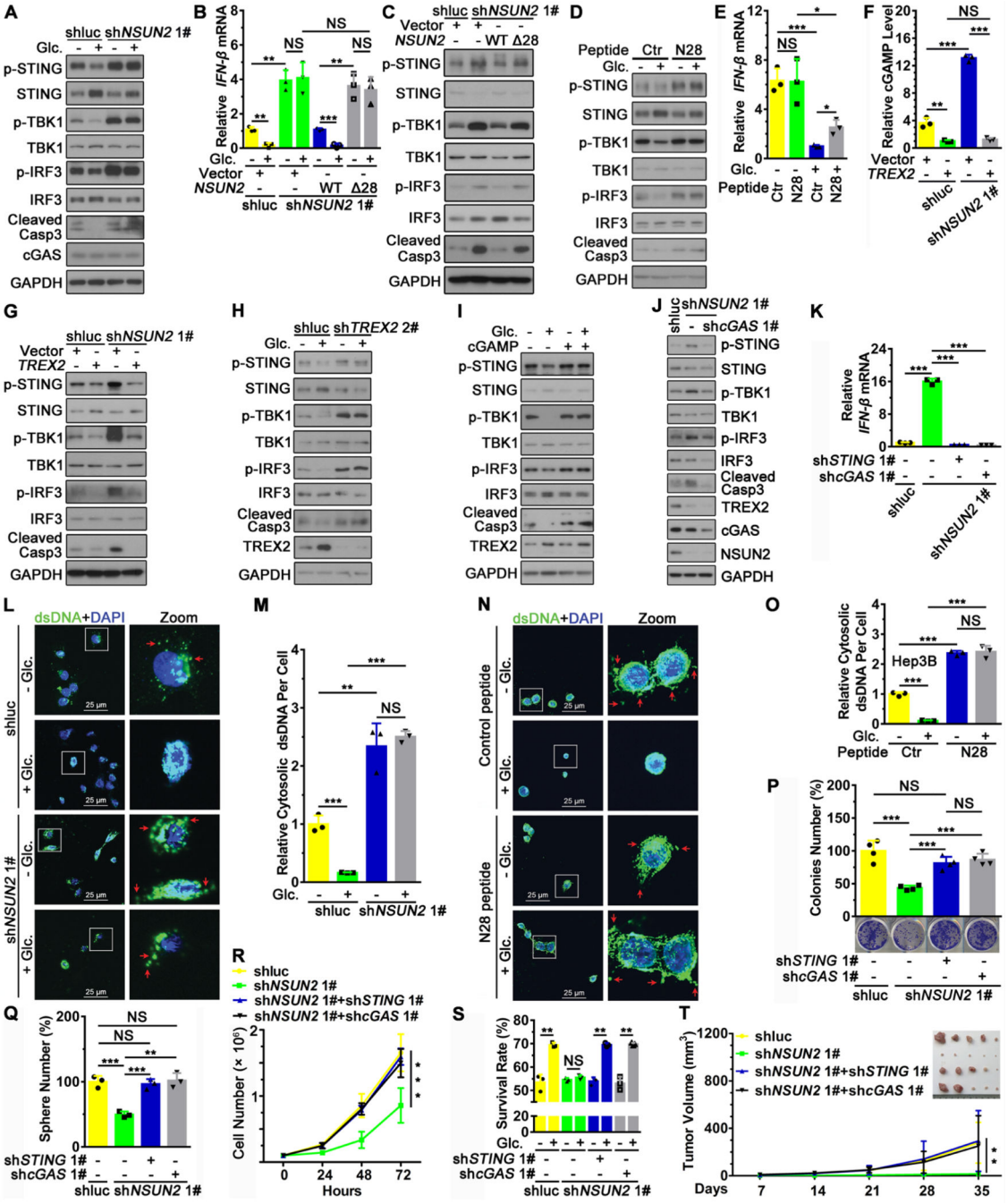

Figure 5. The Glucose/NSUN2/TREX2 Axis Restricts Cytosolic dsDNA Accumulation for cGAS/STING Activation to Maintain Oncogenic Activity of Cancer Cells

(A) Immunoblotting in NSUN2 knockdown Hep3B cells glucose-starved for 4 h and restored with glucose (5.5 mM) 2 h (n = 3 biological replicates).

(B) RT-qPCR analysis in NSUN2 knockdown Hep3B cells restored with *NSUN2*-WT or *NSUN2*-Δ28, glucose-starved for 4 h and restored with glucose (5.5 mM) 2 h (n = 3 biological replicates).

(C) Immunoblotting in NSUN2 knockdown Hep3B cells restored with *NSUN2*-WT or *NSUN2*-Δ28 (n = 3 biological replicates).

(D and E) Immunoblotting (D) and RT-qPCR analysis (E) in Hep3B cells glucose-starved for 4 h and restored with glucose (5.5 mM) 2 h along with control or N28 peptide (2 μM) treatment (n = 3 biological replicates).

(F and G) ELISA (F) and immunoblotting (G) in NSUN2 knockdown Hep3B cells restored with or without *TREX2* (n = 3 biological replicates).

(H) Immunoblotting in TREX2 knockdown Hep3B cells glucose-starved for 4 h and restored with glucose (5.5 mM) 2 h (n = 3 biological replicates).

(I) Immunoblotting in Hep3B starved with glucose and restored for 4 h with glucose (5.5 mM) 2 h along with or without cGAMP (1 μM) (n = 3 biological replicates).

(J) Immunoblotting in shluc, sh*NSUN2* and sh*NSUN2*+sh*cGAS* Hep3B cells (n = 3 biological replicates).

(K) RT-qPCR analysis in shluc, sh*NSUN2*, sh*NSUN2*+sh*STING* and sh*NSUN2*+sh*cGAS* Hep3B cells (n = 3 biological replicates).

(L and M) Confocal images (L) and quantification (M) of cytosolic dsDNA in NSUN2 knockdown Hep3B cells glucose-starved for 4 h and restored with glucose (5.5 mM) 2 h (n = 3 biological replicates).

(N and O) Confocal images (N) and quantification (O) of cytosolic dsDNA in Hep3B cells glucose-starved for 4 h and restored with glucose (5.5 mM) 2 h along with control or N28 peptide (2 μM) treatment. Scale bar, 25 μm (n = 3 biological replicates).

(P, Q, R, and S) Colony forming assays (P), sphere forming assays (Q), growth curve (R) and survival rate (S) in shluc, sh*NSUN2*, sh*NSUN2*+sh*STING*, or sh*NSUN2*+sh*cGAS* Hep3B cells (n = 3 biological replicates).

(T) *In vivo* xenograft tumorigenesis assays of shluc, sh*NSUN2*, sh*NSUN2*+sh*STING* and sh*NSUN2*+sh*cGAS* Hep3B cells subcutaneously inoculated in nude mice (n = 5 animals/group).

Data are mean ± SD. *, $p < 0.05$, **, $p < 0.01$, ***, $p < 0.001$, NS, non-significant by Student's *t*-test (B, E, F, K, M, O, P, Q, S) or by 2-way ANOVA (R, T). See also Figure S6–S9.

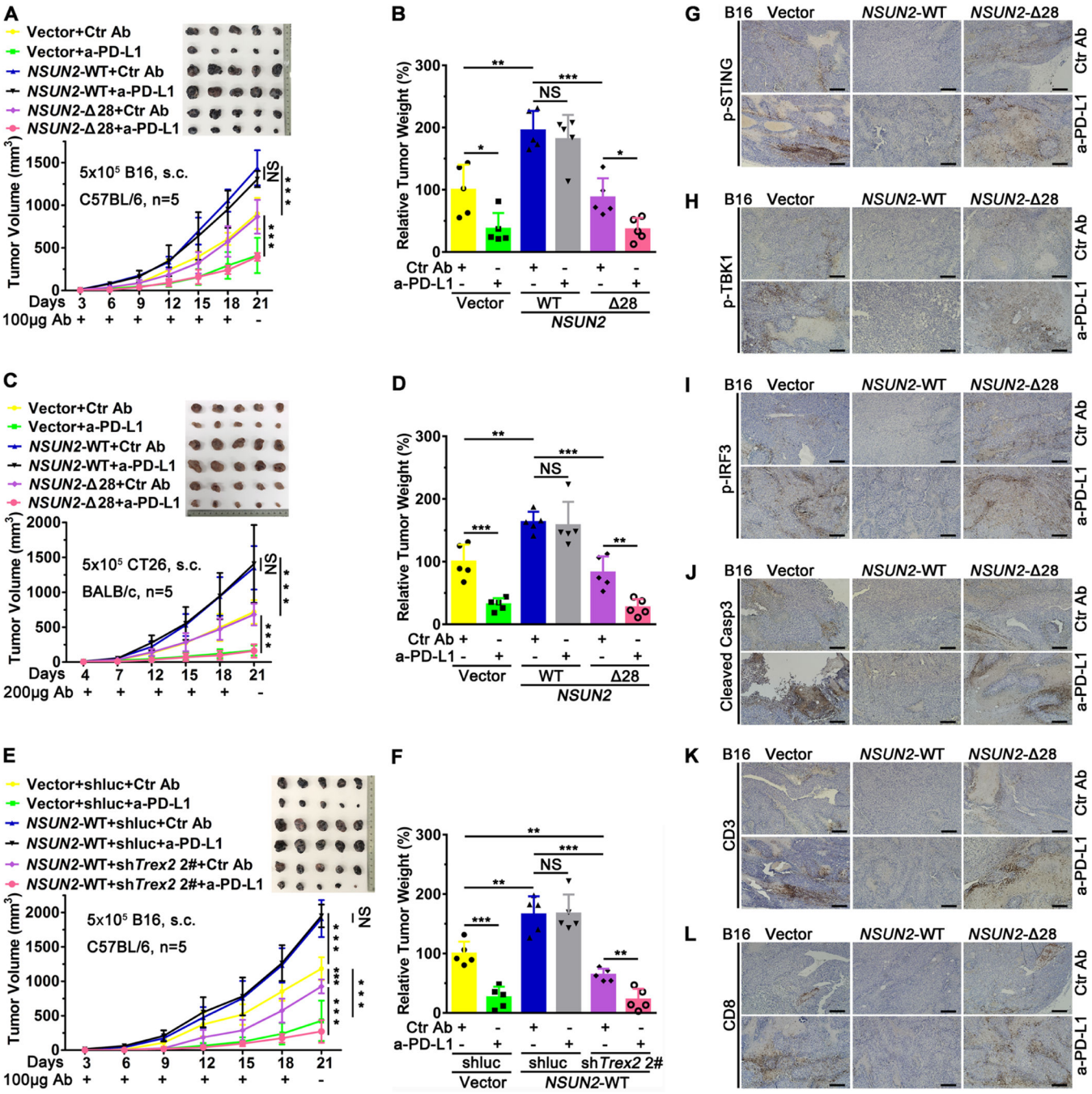

Figure 6. The Glucose/NSUN2/TREX2 Axis Drives cGAS/STING Signaling Repression to Promote Anti-PD-L1 Immunotherapy Resistance by Restricting Apoptosis and CD8$^+$ T Cell Infiltration

(A, B, and G-L) Tumor volume (A), tumor weight (B), immunohistochemistry for p-STING (G), p-TBK1 (H), p-IRF3 (I), cleaved caspase-3 (J), CD3 (K), and CD8 (L) *in vivo* allograft tumorigenesis assays of B16 cells overexpression with Vector control, *NSUN2*-WT or *NSUN2*-Δ28 inoculated in C57BL/6 mice (n = 5 animals/group), treated with anti-mouse PD-L1 or rat IgG2b isotype control antibodies. Scale bar, 200 μm.

(C and D) Tumor volume (C) and tumor weight (D) *in vivo* allograft tumorigenesis assays of CT26 cells overexpression with Vector control, *NSUN2*-WT or *NSUN2*-Δ28 inoculated in BALB/c mice (n = 5 animals/group), treated with anti-mouse PD-L1 or rat IgG2b isotype control antibodies.

(E and F) Tumor volume (E) and tumor weight (F) *in vivo* allograft tumorigenesis assays of Vector+shluc, *NSUN2*-WT+shluc and *NSUN2*-WT+sh*Trex2* B16 cells inoculated in C57BL/6 mice (n = 5 animals/group), treated with anti-mouse PD-L1 or rat IgG2b isotype control antibodies.

Data are mean ± SD. *, $p < 0.05$, **, $p < 0.01$, ***, $p < 0.001$, NS, non-significant by Student's *t*-test (B, D, F) or by 2-way ANOVA (A, C, E). See also Figure S10.

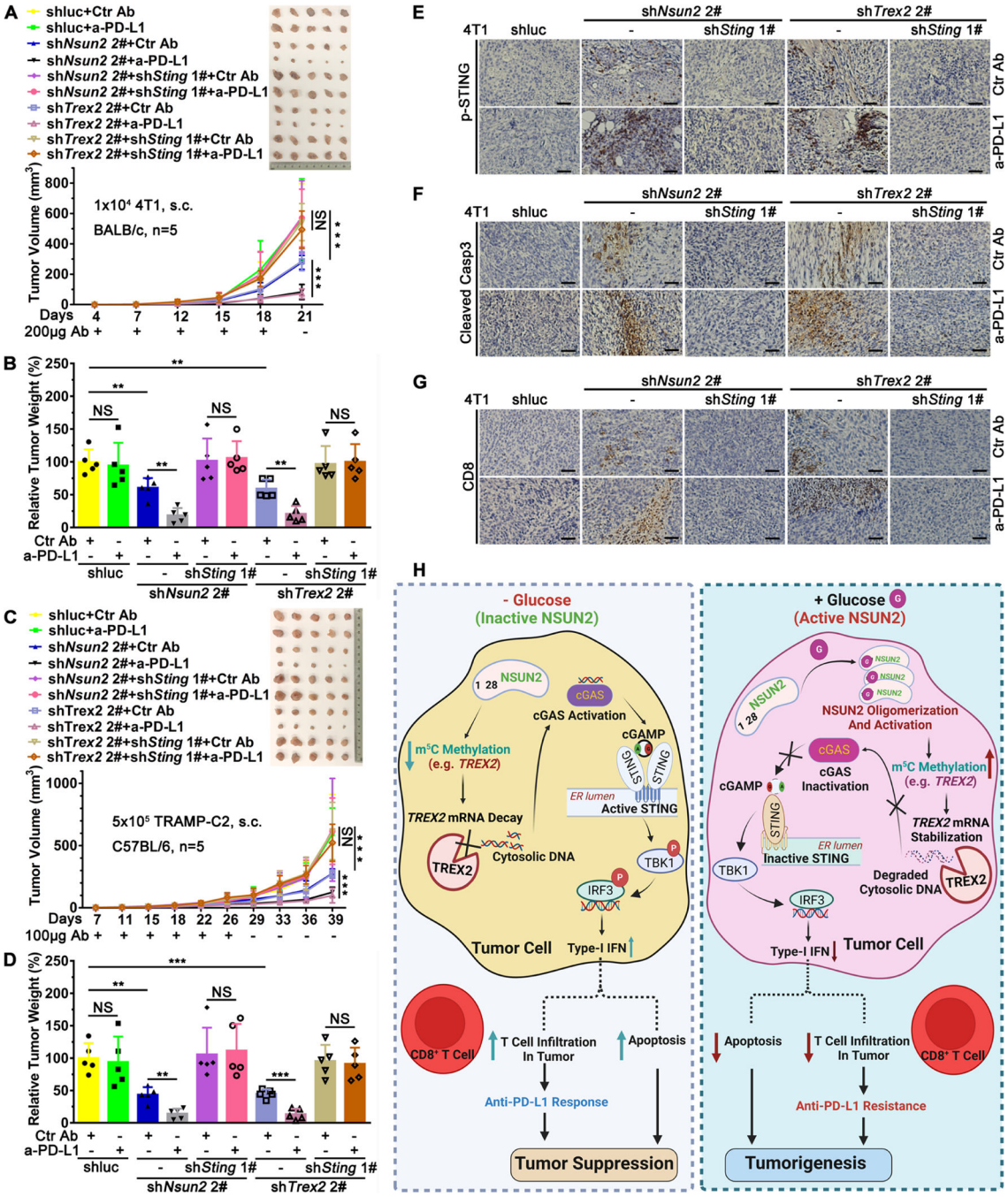

Figure 7. Targeting The Glucose/NSUN2/TREX2 Axis Overcomes Anti-PD-L1 Immunotherapy Resistance through cGAS/STING Activation for Apoptosis and CD8$^+$ T Cell Infiltration

(A, B, E, F, and G) Tumor volume (A), tumor weight (B), immunohistochemistry for p-STING (E), cleaved caspase-3 (F), and CD8 (G) *in vivo* allograft tumorigenesis assays of shluc, sh*Nsun2*, sh*Nsun2*+sh*Sting*, sh*Trex2*, and sh*Trex2*+sh*Sting* 4T1 cells injected in BALB/c mice (n = 5 animals/group), treated with anti-mouse PD-L1 or rat IgG2b isotype control antibodies. Scale bar, 50 μm.

(C and D) Tumor volume (C) and tumor weight (D) *in vivo* allograft tumorigenesis assays of shluc, sh*Nsun2*, sh*Nsun2*+sh*Sting*, sh*Trex2*, and sh*Trex2*+sh*Sting* TRAMP-C2 cells injected

in C57BL/6 mice (n = 5 animals/group), treated with anti-mouse PD-L1 or rat IgG2b isotype control antibodies.

(H) Illustration of the glucose sensing mechanism by NSUN2, which serves as a glucose sensor whose activation by glucose drives m^5C RNA methylation and mRNA stability of *TREX2* leading to cGAS/STING repression and subsequent tumor promotion and immunotherapy resistance.

Data are mean ± SD. *, $p < 0.05$, **, $p < 0.01$, ***, $p < 0.001$, NS, non-significant by Student's *t*-test (B, D) or by 2-way ANOVA (A, C). See also Figure S11.

Key Resources Table

REAGENT or RESOURCE	SOURCE	IDENTIFIER
Antibodies		
NSUN2 Monoclonal antibody	Proteintech	Cat# 66580–1-Ig; RRID: AB_2881940
NSUN2 Polyclonal antibody	Proteintech	Cat# 20854–1-AP; RRID: AB_10693629
DDX21 Polyclonal antibody	Proteintech	Cat# 10528–1-AP, RRID:AB_2092705
Mouse monoclonal anti-HIV-TAT(N3)	abcam	Cat# ab63957; RRID: AB_1139536
Recombinant Anti-CD3 antibody [SP162]	abcam	Cat# ab135372; RRID:AB_2884903
Recombinant Anti-CD8 alpha antibody [CAL38]	abcam	Cat# ab237723; RRID:AB_2864723
5-Methylcytosine (5-mC) (D3S2Z) Rabbit mAb	Cell Signaling Technology	Cat# 28692; RRID:AB_2798962
Oct-4 antibody	Cell Signaling Technology	Cat# 2750S; RRID: AB_823583
Sox2 (D6D9) XP® Rabbit mAb	Cell Signaling Technology	Cat# 3579S; RRID:AB_2195767
Phospho-STING (Ser366) (D7C3S) Rabbit mAb	Cell Signaling Technology	Cat# 19781; RRID:AB_2737062
STING (D2P2F) Rabbit mAb	Cell Signaling Technology	Cat# 13647s; RRID:AB_2732796
Rabbit monoclonal anti-TBK1(phosS172) (D52C2)	Cell Signaling Technology	Cat# 5483; RRID: AB_10693472
Rabbit monoclonal anti-IRF3(phosS396) (4D4G)	Cell Signaling Technology	Cat# 4947; RRID: AB_823547
Cleaved Caspase-3 (Asp175) (5A1E) Rabbit mAb	Cell Signaling Technology	Cat# 9664; RRID:AB_2070042
Phospho-STING (Ser365) (D1C4T) Rabbit mAb	Cell Signaling Technology	Cat# 62912; RRID:AB_2799635
Phospho-IRF-3 (Ser396) (D6O1M) Rabbit mAb	Cell Signaling Technology	Cat# 29047; RRID:AB_2773013
Phospho-AMPKα (Thr172) (D4D6D) Rabbit mAb	Cell Signaling Technology	Cat#50081; RRID: AB_2799368
AMPKα Antibody	Cell Signaling Technology	Cat# 2532, RRID:AB_330331
Phospho-Histone H2A.X (Ser139) Antibody #2577	Cell Signaling Technology	Cat# 2577, RRID:AB_2118010
Anti-DNA, single stranded, clone TNT-3	Millipore	Cat# MAB3868, RRID:AB_570342
Mouse monoclonal anti-HK2 (B-8)	Santa Cruz Biotechnology	Cat# sc-374091; RRID: AB_10917915
Anti-TREX-2 Antibody (E-4)	Santa Cruz Biotechnology	Cat# sc-390890
Anti-TREX-1 Antibody (E-6)	Santa Cruz Biotechnology	Cat# sc-271870; RRID:AB_10708266
NeuroD2 (G-10) Antibody	Santa Cruz Biotechnology	Cat# sc-365896; RRID:AB_10843361
GST (clone B-14)	Santa Cruz Biotechnology	Cat#sc-138; RRID: AB_627677
Anti-Neuregulin-2 Antibody (A-12) (NRG2)	Santa Cruz Biotechnology	Cat# sc-398594
Anti-PKC γ Antibody (C-4)	Santa Cruz Biotechnology	Cat# sc-166385; RRID:AB_2018059
Anti-HES2 Antibody (H-8)	Santa Cruz Biotechnology	Cat# sc-514711
Anti-SREBP-1 Antibody (2A4)	Santa Cruz Biotechnology	Cat# sc-13551; RRID:AB_628282
Anti-HNF-4α Antibody (H-1)	Santa Cruz Biotechnology	Cat# sc-374229; RRID:AB_10989766
Anti-cGAS Antibody (D-9)	Santa Cruz Biotechnology	Cat# sc-515777; RRID:AB_2734736
Anti-TBK1 Antibody (108A429)	Santa Cruz Biotechnology	Cat# sc-52957; RRID:AB_783995
Anti-IRF-3 Antibody (SL-12)	Santa Cruz Biotechnology	Cat# sc-33641; RRID:AB_627826
Anti-ds DNA Marker Antibody (HYB331–01)	Santa Cruz Biotechnology	Cat# sc-58749; RRID:AB_783088
Mouse monoclonal anti-β-Actin(C4)	Santa Cruz Biotechnology	Cat# sc-47778; RRID: AB_626632
SLC47A2 Polyclonal Antibody	Thermo Fisher	Cat# PA5–37989

REAGENT or RESOURCE	SOURCE	IDENTIFIER
SLC9A2 Polyclonal Antibody	Thermo Fisher	Cat# PA5–80034
PAX6 Monoclonal Antibody (AD2.38), eBioscience™	Thermo Fisher	Cat# 14–9914-82; RRID: AB_10669586
Alexa Fluor 488 anti-mouse IgG	Thermo Fisher	Cat# A-21202; RRID: AB_141607
GAPDH (clone GAPDH-71.1)	Sigma-Aldrich	Cat# G8795; RRID: AB_1078991
Tubulin (clone AA13)	Sigma-Aldrich	Cat# T8203; RRID: AB_1841230
HRP-AffiniPure Goat Anti-Mouse IgG (H+L)	jacksonimmuno	Cat# 115–035-003; RRID: AB_10015289
HRP-AffiniPure Goat Anti-Rabbit IgG (H+L)	jacksonimmuno	Cat# 111–035-003; RRID: AB_2313567
InVivoMAb anti-mouse PD-L1 (B7-H1, Clone 10F.9G2)	BioXcell	Cat# BE0101; RRID: AB_10949073
InVivoMAb rat IgG2b isotype control, anti-keyhole limpet hemocyanin (Clone LTF-2)	BioXcell	Cat# BE0090; RRID: AB_1107780
Bacterial and virus strains		
DH5a	Hui-Kuan Lin lab	N/A
Top10	Hui-Kuan Lin lab	N/A
BL21	Hui-Kuan Lin lab	N/A
Chemicals, peptides, and recombinant proteins		
D-(+)-Glucose (Glc.)	Sigma-Aldrich	Cat# G7021
2-Deoxy-D-glucose (2-DG)	Sigma-Aldrich	Cat# D8375
D-Fructose 6-phosphate disodium salt hydrate (F6P)	Sigma-Aldrich	Cat# F3627–500MG
D-Fructose 1,6-bisphosphate trisodium salt hydrate (FBP)	Sigma-Aldrich	Cat# F6803–1G
D-Glucose 6-phosphate sodium salt (G6P)	Sigma-Aldrich	Cat# G7879–1G
Myo-inositol (Ins)	Sigma-Aldrich	Cat# I7508
Sodium acetate	Sigma-Aldrich	Cat# S2889–250G
Methylene blue	Sigma-Aldrich	Cat# M9140–25G
Formamide	Sigma-Aldrich	Cat# F9037–100ML
Polybrene Diethyl pyrocarbonate	Sigma-Aldrich	Cat# D5758–25ML
Aprotinin	Sigma-Aldrich	Cat# A1153–5MG
Actinomycin D (Act. D)	Sigma-Aldrich	Cat# A1410–5MG
Citrate Buffer, pH 6.0, 10×, Antigen Retriever	Sigma-Aldrich	Cat# C9999–1000ML
Acid hematoxylin solution	Sigma-Aldrich	Cat# 2852–100ML
3-O-methyl-D-glucopyranose	Sigma-Aldrich	Cat# M4879–10G
compound C (Dorsomorphin)	Sigma-Aldrich	Cat# P5499–5MG
Leupeptin (hemisulfate)	Cayman	Cat# 103476–89-7
2’3’-cGAMP	Invivogene	Cat# tlrl-nacga23–02
ADENOSYL-L-METHIONINE, S-[METHYL-3H] (3H SAM)	American radiolabelled	Cat# ART 0288–250 μCi
Glutathione Sepharose® 4B	GE/vwr	Cat# 17–0756-01
PreScission Protease	GE/vwr	Cat# 27084301
Native Sample Buffer for Protein Gels	Bio-RAD	Cat# 1610738
PrimeScript RT Master Mix	Takara	Cat# DRR036A
2x SYBR Green qPCR Master Mix	BIMAKE	Cat# B21203
Control peptide	This paper	N/A

REAGENT or RESOURCE	SOURCE	IDENTIFIER
N28 peptide	This paper	N/A
Bio-glucose	This paper	N/A
InVivoPure pH 6.5 Dilution Buffer	BioXcell	Cat# IP0065
InVivoPure pH 7.0 Dilution Buffer	BioXcell	Cat# IP0070
Hydrogen Peroxide Blocking Reagent	Abcam	Cat# ab64218
Normal Goat Serum	Abcam	Cat# ab7481
Amersham Hybond-N+ Western Blotting Membrane	GE Healthcare	Cat# RPN303B
Glucose-free DMEM	Gibco	Cat# 11966–025
dialyzed FBS (US origin)	Gibco	Cat# 26400044
B-27™ Supplement (50X), serum free	Thermo Fisher	Cat# 17504044
RNasin® Plus Ribonuclease Inhibitor	Promega/fisher	Cat# N2615
SureBeads™ Protein A Magnetic Beads	Bio-Rad	Cat# 1614013
SILAC Advanced DMEM/F-12 Flex Media (no glucose, , no phenol red)	Thermo Fisher	Cat# A2494301
MgCl2 (1 M, RNase-free)	Thermo Fisher	Cat# AM9530G
M-PER™ Mammalian Protein Extraction Reagent	Thermo Fisher	Cat# PI78503
DMEM/F-12 Medium	Hyclone	Cat# SH30261.01
DMEM-HI	FISHER	Cat# SH30243FS
RPMI-1640	FISHER	Cat# A10491–01
PBS	FISHER	Cat# BW17–516F24
Nuclease-Free Water (not DEPC-Treated)	FISHER	Cat# AM9930
Tissue-Tek Glas™ mounting medium	FISHER	Cat# NC9016679
Scott’s bluing reagent	FISHER	Cat# 6697–32
Xylenes (Histological), Fisher Chemical™	FISHER	Cat# X3P-1GAL
Lipofectamine™ 3000 Transfection Reagen	FISHER	Cat# L3000015
Dynabeads MyOne Streptavidin T1	Thermo Fisher Scientific	Cat# 65601
Bismaleimide Crosslinkers (BMH)	Thermo	Cat# 22330
Pyruvate (Pyr)	Thermo	Cat# 10569010
Critical commercial assays		
ATP Determination Kit	Thermo Fisher	Cat# A22066
2′3′-cGAMP competitive ELISA assay Kit	Cayman	Cat# 501700
DAB Substrate Kit	Abcam	Cat# ab64238
Quick-RNA™ Miniprep Kit	ZYMO Research	Cat# R1055
RNA Clean & Concentrator-5	ZYMO Research	Cat# R1013
Zymo-Spin™ IIICG Columns (green)	ZYMO Research	Cat# C1006–250-G
HMW Native Marker Kit	GE Healthcare	Cat# C17044501
FITC Annexin V Apoptosis Detection Kit I	BD	Cat# 556547
Human Interferon beta ELISA Kit	Abcam	Cat# ab278127
Deposited data		

REAGENT or RESOURCE	SOURCE	IDENTIFIER
Uncropped scans of all blots and all values used to generate graphs	This paper	https://dx.doi.org/10.17632/wnfs2xmgp7.1
Experimental models: Cell lines		
Human: Hep3B	ATCC	Cat# HB-8064
Human: PC3	ATCC	Cat# CRL-1435
Human: HEK293T	ATCC	Cat# CRL-11268
Human: HEK293	Hui-Kuan Lin lab	N/A
Mouse: B16	ATCC	Cat# CRL-6475
Mouse: CT26	ATCC	Cat# CRL-2638
Mouse: 4T1	ATCC	Cat# CRL-2539
Mouse: TRAMP-C2	ATCC	Cat# CRL-2731
Mouse: AMPK$^{-/-}$ mouse embryonic fibroblasts	Dr. Kun-Liang Guan (The University of California, San Diego)	N/A
Experimental models: Organisms/strains		
Nude (Crl:NU(NCr)-Foxn1nu) mice	Charles Rivers	Code 490
BALB/c (NCI BALB-cAnNCr) mice	Charles Rivers	Code 555
C57BL/6	Charles Rivers	Code 027
Oligonucleotides		
ShRNA:human *NSUN2*-1#	Sigma-Aldrich	Cat# TRCN0000297585
ShRNA:human *NSUN2*-2#	Sigma-Aldrich	Cat# TRCN0000158808
ShRNA:human *HK2*-1#	Sigma-Aldrich	Cat# TRCN0000196260
ShRNA:human *HK2*-2#	Sigma-Aldrich	Cat# TRCN0000195582
ShRNA:human *TREX2*-1#	Sigma-Aldrich	Cat# TRCN0000415200
ShRNA:human *TREX2*-2#	Sigma-Aldrich	Cat# TRCN0000426635
ShRNA:human *cGAS*-1#	Sigma-Aldrich	Cat# TRCN0000128706
ShRNA:human *cGAS*-2#	Sigma-Aldrich	Cat# TRCN0000428336
ShRNA:human *STING*-1#	Sigma-Aldrich	Cat# TRCN0000163029
ShRNA:human *STING*-2#	Sigma-Aldrich	Cat# TRCN0000161345
ShRNA:human *TREX1*-1#	Sigma-Aldrich	Cat# TRCN0000315303
ShRNA:human *TREX1*-2#	Sigma-Aldrich	Cat# TRCN0000315304
ShRNA:mouse *Nsun2*-1#	Sigma-Aldrich	Cat# TRCN0000325347
ShRNA:mouse *Nsun2*-2#	Sigma-Aldrich	Cat# TRCN0000097384
ShRNA:mouse *Trex2*-1#	Sigma-Aldrich	Cat# TRCN0000428474
ShRNA:mouse *Trex2*-2#	Sigma-Aldrich	Cat# TRCN0000077193
ShRNA:mouse *Sting*-1#	Sigma-Aldrich	Cat# TRCN0000346319
ShRNA:mouse *Sting*-2#	Sigma-Aldrich	Cat# TRCN0000346321
qPCR pimers, see Table S3	This paper	N/A
Recombinant DNA		

REAGENT or RESOURCE	SOURCE	IDENTIFIER
pMD2G	Hui-Kuan Lin lab	N/A
pPAX	Hui-Kuan Lin lab	N/A
pGEX-6P-1-*NSUN2*-F1	This paper	N/A
pGEX-6P-1-*NSUN2*-F2	This paper	N/A
pGEX-6P-1-*NSUN2*-F3	This paper	N/A
pGEX-6P-1-*NSUN2*-Δ1–84	This paper	N/A
pGEX-6P-1-*NSUN2*-Δ184–190	This paper	N/A
pGEX-6P-1-*NSUN2*-Δ121–236	This paper	N/A
pGEX-6P-1-*NSUN2*-Δ1–28	This paper	N/A
pGEX-6P-1-*NSUN2*-Δ29–56	This paper	N/A
pGEX-6P-1-*NSUN2*-Δ57–84	This paper	N/A
pFLAG-CMV2-*NSUN2*-F1	This paper	N/A
pFLAG-CMV2-*TREX2*	This paper	N/A
pCDH-blasticidin-*NSUN2*-WT	This paper	N/A
pCDH blasticidin-*NSUN2*-Δ28	This paper	N/A
pCDH blasticidin-*TREX2*	This paper	N/A
Software and algorithms		
ImageJ	ImageJ software	https://login.go.libproxy.wakehealth.edu/login?qurl=https://imagej.nih.gov%2fij%2findex.html
GraphPad.Prism 7	Graphpad software	N/A
Excel	Microsoft	N/A
PowerPoint	Microsoft	N/A
BioRender	BiorRender	app.biorender.com